Measurement report: Vertical and temporal variability of near-surface ozone production rate and sensitivity in an urban area in Pearl River Delta (PRD) region, China

Jun Zhou[1,2#], Chunsheng Zhang[3#], Aiming Liu[3], Bin Yuan[1,2*], Yan Wang[1,2], Wenjie Wang[1,4], Jie-Ping Zhou[1,2], Yixin Hao[1,2], Xiao-Bing Li[1,2*], Xianjun He[1,2], Xin Song[1,2], Yubin Chen[1,2], Suxia Yang[1,2], Shuchun Yang[1,2], Yanfeng Wu[1,2], Bin Jiang[1,2], Shan Huang[1,2], Junwen Liu[1,2], Yuwen Peng[1,2], Jipeng Qi[1,2], Minhui Deng[1,2], Bowen Zhong[1,2], Yibo Huangfu[1,2], Min Shao[1,2*]

[1]Institute for Environmental and Climate Research, Jinan University, Guangzhou 511443, China

[2]Guangdong-Hongkong-Macau Joint Laboratory of Collaborative Innovation for Environmental Quality, Guangzhou 511443, China

[3]Shenzhen National Climate Observatory, Shenzhen 518040, China

[4]Multiphase Chemistry Department, Max Planck Institute for Chemistry, Mainz 55128, Germany

[#]These authors contribute equally to this work.

Correspondence: Bin Yuan (byuan@jnu.edu.cn), Xiao-Bing Li (lixiaobing@jnu.edu.cn), Min Shao (mshao@jnu.edu.cn)

Abstract: Understanding the near-ground vertical and temporal photochemical O_3 formation mechanism is important to mitigate O_3 pollution. Here, we measured the vertical profiles of O_3 and its precursors at six different heights ranging from 5 to 335 m using a newly built vertical observation system in the Pearl River Delta (PRD) region, China. The net photochemical ozone production rate ($P(O_3)_{net}$) and O_3 formation sensitivities at various heights were diagnosed using an observation-based model coupled with the Master Chemical Mechanism (MCM v3.3.1). Moreover, to assess model performance and identify the causative factors behind O_3 pollution episodes, the $P(O_3)_{net}$ was measured at 5 m ground level utilizing a custom-built detection system. In total three O_3 pollution episodes and two non-episodes were captured. The identified O_3 pollution episodes were found to be jointly influenced by both photochemical

production and physical transport, with local photochemical reactions playing a major role. The high index of agreement (IOA) calculated from comparing the modelled and measured $P(O_3)_{net}$ values indicated the rationality to investigate the vertical and temporal variability of O_3 formation mechanisms using modelling results. However, the measured $P(O_3)_{net}$ values were generally higher than the modelled $P(O_3)_{net}$ values, particularly under high NOx conditions, which may indicate a potential underestimation of total RO_2 by the model. Throughout the measurement period, the contribution of different reaction pathways to O_3 production remained consistent across various heights, with HO_2+NO as the major O_3 production pathway, followed by RO_2+NO. We observed $P(O_3)_{net}$ decreasing with the increase in measurement height, primarily attributed to the decreased O_3 precursors anthropogenic volatile organic compounds (AVOC) and oxygenated volatile organic compounds (OVOC). O_3 formation regimes were similar at different heights during both episodes and non-episodes, either located in the volatile organic compounds (VOCs) sensitive regime or in the transition regime and more sensitive to VOCs. Diurnally, photochemical O_3 formation typically remained in the VOCs sensitive regime during the morning and noon, but transitioned to the transition regime and more sensitive to VOCs in the afternoon around 16:00 local time (LT). The vertical and temporal O_3 formation is most sensitive to AVOC and OVOC, suggesting that targeting VOCs, especially AVOC and OVOC, for control measures is more practical and feasible at the observation site. The vertical temporal analysis of O_3 formation mechanisms near the ground surface in this study provides critical foundational knowledge for formulating effective short-term emergency and long-term strategies to combat O_3 pollution in the PRD region of China.

1. Introduction

Tropospheric ozone (O_3), which has adverse effects on ecosystems, climate change, and human health (Fiore et al., 2009; Anenberg Susan et al., 2012; Seinfeld, 2016), has become an important factor resulting in severe regional air pollution in China (Zhu et al., 2020). Tropospheric O_3 mainly comes from stratospheric intrusions and the photochemical reactions of O_3 precursors, involving volatile organic compounds (VOCs) and nitrogen oxides (NOx=NO+NO_2). The O_3-precursor relationship can be split into a "NOx-limited" or "VOC-limited" or "mixed-sensitive" regime (Seinfeld and Pandis, 2016; Sillman S., 1999). A "NOx-limited" regime has higher VOCs/NOx ratios and the O_3 formation is sensitive to NOx concentration changes, while a "VOCs-limited"

64 regime has lower VOCs/NOx ratios and the O_3 formation is sensitive to VOCs

65 concentration changes. In a "mixed-sensitive" regime, O_3 formation responds

66 positively to changes in both NOx and VOC emissions (Wang et al., 2019). Local O_3

67 concentrations can be further influenced by meteorological conditions and the regional

68 transport of O_3 and its precursors (Gong and Liao, 2019; Chang et al., 2019). The Pearl

69 River Delta (PRD) stands out as one of the most rapidly developing economic and

70 urbanized regions in China, which currently is suffering from severe ground-level O_3

71 pollution (Lu et al., 2018; Yang et al., 2019). Currently, many scholars have analyzed

72 the relationship between tropospheric O_3 pollution and its precursors and

73 meteorological elements in the PRD region, results show that the surface O_3 pollution

74 is determined by both local photochemistry and physical transport, with long-range

75 transport contributing 30%-70% to surface O_3 concentrations (Mao et al., 2022; Shen

76 et al., 2021; Li et al., 2012, 2013). However, the distribution of O_3 is highly variable at

77 different altitudes (Wang et al., 2021), due to vertical differences in VOCs

78 concentrations and sources, as well as the sensitivity of O_3 formation (Liu et al., 2023;

79 Tang et al., 2017). Due to the presence of strong vertical mixing driven by the surface

80 heating effect in the daytime boundary layer, the budget of the O_3 at the ground level

81 and also at an arbitrary height in the daytime boundary layer is closely related to the

82 formation and removal of O_3 at other heights (Tang et al., 2017). In addition, the

83 difference in vertical gradients of precursors may drive the vertical change in the

84 photochemical formation regimes of O_3 (Zhao et al., 2019). Using data from only one

85 height to understand the photochemical reactions in the planetary boundary layer is of

86 great limitation. Thus, diagnosing the O_3 formation mechanism at different heights is

87 essential to achieve effective control of O_3 pollution.

88 Currently, remote sensing techniques with high time resolution and real-time

89 response, such as lidar and optical absorption spectroscopy, have been utilized to

90 measure the vertical distribution of O_3 (Luo et al., 2020a; Wang et al., 2021). However,

91 in situ measurements of VOCs at various heights primarily rely on offline methods

92 combined with diverse techniques, including aircraft, tethered balloons, tall buildings

93 and towers, unmanned aerial vehicles (UAVs or drones), and satellite observations

94 (Klein et al., 2019; Li et al., 2022; Geng et al., 2020; Benish et al., 2020; Li et al., 2021;

95 Wang et al., 2019). Owing to the low time resolution of these monitoring techniques,

96 achieving continuous vertical coverage of VOCs and NOx measurements is challenging.

97   Consequently, the vertical distribution structure of VOCs remains unclear, thus largely

98   hindering our understanding of the vertical and temporal regional O_3 formation

99   mechanism.

100   To fill the gaps in the existing studies, we utilized a newly constructed vertical

101   observation system based on the Shenzhen Meteorological Gradient Tower (SZMGT)

102   (Li et al., 2023). This system measured the vertical profiles of O_3 and its precursors at

103   six different heights from 5 to 335 m. To diagnose the net O_3 production rate, $P(O_3)_{net}$,

104   and O_3 formation sensitivities across various heights, we employed an observation-

105   based model coupled with the Master Chemical Mechanism (MCM v3.3.1), referred to

106   as OBM-MCM in the following. Additionally, we employed a novel net photochemical

107   O_3 production rate ($P(O_3)_{net}$, NPOPR) detection system to measure the $P(O_3)_{net}$ at the 5

108   m ground level to explore potential reasons for O_3 pollution episodes (Hao et al., 2023),

109   i.e., examine the contribution of chemical and physical processes to changes in O_3

110   concentration. Comparisons between the directly measured $P(O_3)_{net}$ results and the

111   model-derived data enabled us to evaluate the simulation accuracy and explore potential

112   reasons for discrepancies of the OBM-MCM model concerning photochemical O_3

113   formation. Based on these results, we have extensively discussed the vertical and

114   temporal variability in $P(O_3)_{net}$ and O_3 formation sensitivity, while acknowledging

115   potential biases associated to the modelling. The findings of this study offer a new

116   benchmark for understanding the vertical profile of photochemical O_3 formation

117   mechanism, aiding in the identification of the primary driver of ground-level O_3

118   pollution. This identification is crucial as it can provide essential theoretical support for

119   developing short-term effective emergency and long-term control measures targeting

120   O_3 in PRD region of China.

121   **2. Materials and Methods**

122   **2.1 Sampling site**

123   Field measurements were conducted at the Shenzhen Meteorological Gradient

124   Tower (SZMGT) (22.65° N,113.89° E) from November 13 to December 10, 2021. The

125   SZMGT is 365 m high and is currently the tallest mast tower in Asia and the second

126   tallest of this kind in the world. The main structure of the tower is made of steel, steel

127   stray lines are used for fixing and securing the tower. It is located in the Tiegang

128   Reservior Water Reserve at Bao'an District of Shenzhen, in the Pearl River Delta (PRD)

region of China. The area is surrounded by a high density of vegetation, reservoir features, low-rise buildings, and hills/mountains (Luo et al., 2020b).

2.2 Instrumentation

2.2.1 The vertical sampling system

A tower-based observation system for traces gases using long perfluoroalkoxy alkane (PFA) tubing (OD: 1/2") was used to sample the O_3 and O_3 precursors at six heights during the campaign, including 5, 40, 70, 120, 220, and 335 m above the ground. All six tubes were continuously drawn using a rotary vane vacuum pump to keep flushing with ambient air to reduce tube delay of the organic compounds, with the flow rate controlled by critical orifices (orifice diameter: 0.063"). A Teflon solenoid valve group was used to switch the air samples at specified time intervals so that the subsamples from these six heights could be sequentially drawn by instruments (see Fig. S1). Consequently, the flow rates of the air sample streams for the six tubes varied between 12.0 and 15.0 SLPM without subsampling and were less than 20 SLPM with subsampling. The residence time of the sample gas in the longest tube (~ 400 m) is less than 180 s at a flow rate of 13 SLPM. The impacts of long tubing on measurements of various of trace gases, including O_3, NOx, and a set of organic compounds, were systematically investigated using a combination of laboratory tests, field experiments, and modelling techniques. Field observations proved that this observation system is suitable for analyzing spatio-temporal variations of atmospheric trace gases, with many trace gases could be well measured. More details about the establishment and the characterization of this observation system are described elsewhere (Li et al., 2023).

2.2.2 $P(O_3)_{net}$ measurement

During the campaign, the $P(O_3)_{net}$ at the 5 m ground level was measured using the home-made NPOPR detection system, which was built based on the dual-channel reaction chambers technique. The improvement, characterization, and the photochemical O_3 formation mechanism in the reaction and reference chambers of the NPOPR detection system are described in our previous study (Hao et al., 2023). Briefly, the NPOPR detection system consists of reaction and reference chambers with the same geometry and made of quartz glass. The length and inner diameter of the quartz glass cylinder are 700 mm and 190.5 mm, respectively, which resulted in an inner volume of ~ 20 L. The outer surface of the reference chamber was covered with an Ultem film

161 (SH2CLAR, 3 M, Japan) for ultraviolet (UV) protection, which can block sunlight with

162 wavelengths < 390 nm, thus preventing photochemical reactions inside. During the

163 experiment, both the reaction and reference chambers were placed outdoors and directly

164 exposed to sunlight to simulate real ambient photochemical reactions. Ambient air was

165 introduced into the reaction and reference chambers at the same flow rate, and a Teflon

166 filter was mounted before the chamber inlet to remove fine particles. To correct for the

167 effect of fresh NO titration to O_3, we use O_X (=O_3+NO_2) instead of O_3 to quantify the

168 O_3 generated by photochemical reactions (Pan et al., 2015; Tan et al., 2018). A stream

169 of air from the two chambers was alternately introduced into an NO-reaction chamber

170 every 2 min to convert O_3 in the air to NO_2 in the presence of high concentrations of

171 NO (O_3+NO→NO_2), and the Ox concentrations from the outlet NO-reaction chamber,

172 i.e., the total NO_2 concentrations including the inherent NO_2 in the ambient and that

173 converted from O_3, were measured by a Cavity Attenuated Phase Shift (CAPS) NO_2

174 Monitor (Aerodyne research, Inc., Billerica MA, USA) to avoid other nitrogen oxide

175 interferences to the NO_2 measurement (such as alkyl nitrates, peroxyacyl nitrates,

176 peroxynitric acid, nitrogen pentoxide, etc.). $P(O_3)_{net}$ was obtained by dividing the

177 difference between the Ox concentrations in the reaction and reference chambers (ΔOx)

178 by the mean residence time of air in the reaction chamber $\langle\tau\rangle$:

179 $$P(O_3)_{net} = P(O_X)_{net} = \frac{\Delta O_x}{\tau} = \frac{[O_x]_{reaction} - [O_x]_{reference}}{\tau} \qquad (1)$$

180 A schematic of the NPOPR detection system is shown in Fig. S2. The pulse

181 experiments were performed to quantify the residence time in the chambers (Hao et al.,

182 2023).

183 [Ox] values plugged in Eq. (1) to derive $P(O_3)_{net}$ are measured values corrected

184 for wall losses of Ox and the light-enhanced loss of O_3 (d[O_3]) in the reaction and

185 reference chambers during daytime (Hao et al., 2013):

186 $$\gamma = \frac{d[O_3] \times D}{\omega \times [O_3] \times \tau} \qquad (2)$$

187 where γ is the light-enhanced loss coefficient of O_3, which is derived from $J(O^1D)$

188 according to the relationship obtained from the outdoor experiments (for more details,

189 see supplementary materials: Sect. S3). d[O_3] represents the difference between the O_3

190 mixing ratios at the inlet and outlet of the reaction and reference chambers, D is the

191 diameter of the chambers, ω is the average velocity of O_3 molecules, $[O_3]$ is the injected
192 O_3 mixing ratio at the inlet of the reaction and reference chambers, and τ is the average
193 residence time of the air in the reaction and reference chambers. When quantifying the
194 light-enhanced O_3 loss ($d[O_3]$) during the ambient air measurement, we first calculate
195 γ using the measured $J(O^1D)$ and the γ-$J(O^1D)$ equations listed in Fig. S8 in the
196 reaction and reference chambers, then use the measured $[O_3]$ and Eq. (2) to calculate
197 $d[O_3]$. The results show that such kind of correction can increase the measured $P(O_3)_{net}$
198 by 10% (25% percentile) to 24% (75% percentile), with a median of 17%.

199 The limit of detection (LOD) of the NPOPR detection system is 2.3 ppbv h^{-1} at the
200 sampling air flow rate of 5 L min^{-1}, which is obtained as three times the measurement error of
201 $P(O_3)_{net}$ (Hao et al., 2013). The measurement error of $P(O_3)_{net}$ is determined by the estimation
202 error of Ox in the reaction and reference chambers, which includes the measurement error
203 associated with the O_X of the CAPS-NO_2 monitor and the error due to the light-enhanced loss
204 of O_3. This collective measurement error is referred to as the measurement precision of the
205 NPOPR detection system, with further details provided in the supplementary materials,
206 specifically in Sect. S4. The measurement accuracy of the NPOPR detection system is
207 determined as 13.9 %, representing the maximum systematic error resulting from
208 photochemical O_3 production in the reference chamber. Our earlier research indicated that the
209 modelled $P(O_3)_{net}$ in the reaction chamber is similar to that modelled in ambient air, with the
210 modelled $P(O_3)_{net}$ in the reference chamber accounting for 0-13.9% of that in the reaction
211 chamber (Hao et al., 2023). This is due to the UV protection Ultem film covered on the
212 reference chamber, which only filtered out the sunlight with wavelengths < 390 nm, allowing
213 photochemical O_3 production persist at the sunlight wavelength between 390 nm and 790 nm.
214 Here, we have utilized the same modelling approach described in Hao et al. (2013) to quantify
215 the $P(O_3)_{net}$ in the reference chamber and corrected for the bias introduced by the measurement
216 accuracy.

2.2.3 VOCs measurement

218 VOCs were measured using a high-resolution proton transfer reaction time-of-
219 flight mass spectrometer (PTR-TOF-MS, Ionicon Analytik, Austria) (Wang et al.,
220 2020a; Wu et al., 2020) and an off-line gas chromatography mass spectrometry flame
221 ionization detector (GC-MS-FID) (Wuhan Tianlong, Co. Ltd, China) (Yuan et al.,
222 2012). The concentrations of oxygenated VOCs (OVOC), including formaldehyde
223 (HCHO) and acetaldehyde (CH_3CHO), were measured via PTR-TOF-MS, and the non-
224 methane hydrocarbons (NMHC) were measured via GC-MS-FID. PTR-TOF-MS was

225 run with both hydronium ion (H_3O^+) (Yuan et al., 2017; Wu et al., 2020) and nitric

226 oxide ion (NO^+) (Wang et al., 2020) modes. The measurement error of PTR-TOF-MS

227 was lower than 20%, more details of the PTR-TOF-MS technique can be found in our

228 previous publication (Yuan et al., 2017). The H_3O^+ and NO^+ modes were automatically

229 switched with 20 min H_3O^+ mode and 10 min NO^+ mode. The background signal of

230 each mode was measured every 30 min for at last 2 min by automatically switching the

231 ambient measurement to a custom-built platinum catalytic converter heated to 365 ^oC.

232 Operating the PTR-ToF-MS instrument in NO^+ mode primarily detects higher alkanes,

233 which are known significantly contribute to the formation of secondary organic aerosols

234 (SOA) but negligible contributions to photochemical O_3 formation (Wang et al., 2020).

235 Eventually, we only used VOCs measured during the H_3O^+ mode, which was operated

236 at a drift tube pressure of 3.8 mbar, a temperature of 120 ^oC, and a voltage of 760 V,

237 resulting in an E/N (E refers to the electric field and N refers to the number density of

238 the buffer gas in the drift tube) value of ~ 120 Td (townsend). 3035 ions with m/z up to

239 510 were obtained at time resolutions of 10 s. A gas standard with 35 VOC species was

240 used for calibrations of the PTR-ToF-MS once per day. Raw data from PTR-TOF-MS

241 were analyzed using Tofware software (Tofwerk AG, v3.0.3). Due to the humidity

242 dependencies of various VOCs signals of the PTR-ToF-MS observed in laboratory

243 studies, such as formaldehyde, benzene, methanol, ethanol, and furan (Wu et al., 2020),

244 we determined their humidity-dependence curves. During data analysis, we removed

245 the impacts of ambient humidity change on the measured signals of the PTR-ToF-MS

246 according to these humidity-dependence curves. For the off-line GC-MS-FID

247 measurement, whole-air samples were collected using 3.2 L electro-polished stainless-

248 steel canisters (Entech, USA) at 5 and 120 m at time intervals of two hours. Two

249 automatic canister samplers connected to 12 canisters were used to collect the whole-

250 air samples, with each of canister collecting the sample for 10 min. The canisters were

251 analyzed within one week (Zhu et al., 2018). The concentrations of 56 NMHC species

252 in the canister analyzed by GC-MS/FID were calibrated daily using the mixture of a

253 photochemical assessment monitoring stations (PAMS) standard gas and pure N_2. In

254 addition, the mixture of PAMS standard gas and pure N_2 with species concentrations

255 of 1 ppbv was injected into the analytical system every 10 samples to check the

256 operational stability of the instrument. Pure N_2 was injected into the analytical system

257 at the start and end of each day's analysis to provide reference blank measurements. A

258 full list of all 56 non-methane hydrocarbons (NMHCs) can be found in the

259   supplementary material (Table S2).

2.2.4   Other parameters

261   The photolysis frequencies of different species were measured using the actinic
262   flux spectrometer (PFS-100, Focused Photonics Inc, China). O_3, CO, and NO_X
263   concentrations were measured by a 2B O_3 monitor based on dual-channel UV-
264   absorption (Model 205, 2B Technologies, USA), a gas filter correlation (GFC) CO
265   analyzer (Model 48i, Thermo Fisher Scientific, USA), and a chemiluminescence NOx
266   monitor (Model 42i, Thermo Fisher Scientific, USA), respectively. According to our
267   test (Zhou et al., 2025), a 5% overestimation could be caused in the NO_2 measurement
268   using the chemiluminescence technique compared to the CAPS technique, due to some
269   NO_Z species (i.e., HNO_3, peroxyacetyl nitrate (PANs), HONO, etc.)(Dunlea et al.,
270   2007), this will result in a decrease of the modelled $P(O_3)_{net}$ by < 4%, which is
271   negligible compared to the bias caused by the $P(O_3)_{net}$ in the reference chamber (~ 14%)
272   (Zhou et al., 2023).Temperature (T), relative humidity (RH), and pressure (P) were
273   measured by a portable weather station (Met Pak, Gill Instruments Ltd, UK).

2.3 Data analysis

2.3.1   Observation-based chemical box model

276   We investigated the detailed photochemical O_3 formation mechanism during the
277   observation period based on the field observed data. The specific tropospheric O_3
278   photochemical formation process involves the photolysis of NO_2 at < 420 nm
279   (Sadanaga et al., 2017). Simultaneously, RO_X (RO_X=OH+HO_2 +RO_2) radical recycles
280   provide HO_2 and RO_2 to oxidize NO to NO_2, resulting in the accumulation of O_3 (Shen
281   et al., 2021; Cazorla and Brune, 2010; Sadanaga et al., 2017). Therefore, the ROx
282   radicals and the O_3, OH, NO_3 oxidants play important roles in photochemical O_3
283   formation. A zero-dimensional box model based on the Framework for 0-D
284   Atmospheric Modelling (F0AM) v3.2 (Wolfe et al., 2016) coupled with the MCM
285   v3.3.1 was used to simulate the $P(O_3)_{net}$. MCM v3.1.1 contains a total of 143 VOCs,
286   more than 6700 species, involving more than 17000 reactions (Jenkin et al., 2015).
287    $P(O_3)_{net}$ and O_3 concentrations were simulated by constraining T, RH, P, organic and
288   inorganic substances in gases, including 12 OVOCs (methanol, ethanol, formaldehyde,
289   acetaldehyde, acrolein, acetone, hydroxyacetone, phenol, m-cresol, methyl vinyl ketone,
290   methacrylaldehyde, methyl ethyl ketone), 56 NMHCs (toluene, benzene, isoprene,

291 styrene, etc. as listed in Table S2), inorganic gaseous pollutants (O_3, NO, NO_2, and CO),

292 and photolysis rate values ($J(O^1D)$, $J(NO_2)$, $J(H_2O_2)$, $J(HONO)$, $J(HCHO\_M)$,

293 $J(HCHO\_R)$, $J(NO_3\_M)$, $J(NO_3\_R)$, etc.). The VOCs, NOx, T, RH and P were

294 constrained throughout the modelling period, while O_3 was not constrained after

295 providing initial concentration values. To avoid the build-up of long-lived species to

296 unreasonable levels, we also considered the physical dilution process by setting a

297 constant dilution factor of 1/43200 s^{-1} throughout the modelling period (Liu et al., 2021;

298 Decker et al., 2019). Additionally, the dry deposition rate of O_3 was set to 0.42 cm s^{-1},

299 and the background of O_3, CO, and CH_4 were set to 30, 70, and 1800 ppbv, respectively,

300 based on the findings of Wang et al. (2011), Wang et al. (2022a), and WMO greenhouse

301 gas bulletin (2022). The modelling was run in a time-dependent mode with a resolution

302 of 5 min, and it was run for spin-up time of 72 h to establish steady-state concentrations

303 for secondary pollutants that were not constrained during the simulation. $P(O_3)_{net}$ can

304 be expressed by the difference between O_3 production rate ($P(O_3)$) and O_3 destruction

305 rate ($D(O_3)$), where $P(O_3)$ and $D(O_3)$ can be calculated as Eq. (3)-(4):

306 $$P(O_3) = k_{HO_2+NO}[HO_2][NO] + \sum_i k_{RO_{2,i}+NO}[RO_{2i}][NO]\varphi_i \tag{3}$$

307 $$D(O_3) = k_{O(^1D)+H_2O}[O(^1D)][H_2O] + k_{OH+O_3}[OH][O_3] + k_{HO_2+O_3}[HO_2][O_3]$$

308 $$+ k_{O_3+alkenes}[O_3][alkenes] + k_{OH+NO_2}[OH][NO_2] +$$

309 $$k_{RO_{2,i}+NO_2}[RO_{2i}][NO_2] \tag{4}$$

310 where k_{M+N} represents the bimolecular reaction rate constant of M and N, the

311 subscript 'i' refers to different types of RO_2, and φ_i is the yield of NO_2 of the reaction

312 RO_{2i}+NO. The relevant reaction rates of $P(O_3)$ and $D(O_3)$ and the mean measured

313 concentrations of each VOC category at 5 m ground during O_3 episodes and non-

314 episodes used in the model are listed in Tables S1 and S2.

2.3.2 Derive contribution of chemical and physical processes to O3 changes on the ground level

317 It is known that chemical and physical processes jointly influence the O_3

318 concentration changes near the ground surface (Xue et al., 2014; Tan et al., 2019). The

319 direct measurement of $P(O_3)_{net}$ gave us a chance to identify the contribution of chemical

320 and physical processes to the variation of observed O_3 concentrations using the

321 following equation:

$$\frac{dO_X}{dt} = P(O_X)_{net} + R(O_X)_{trans} \tag{5}$$

Where $\frac{dO_X}{dt}$ is the change rate of the observed O_x mixing ratio change (ppbv h^{-1}), $P(Ox)_{net}$ denotes the net photochemical O_3 production rate (ppbv h^{-1}), which was equal to $P(O_3)_{net}$ and measured directly by the NPOPR system. $R(O_X)_{trans}$ represents O_3 mixing ratio change due to physical transportation (ppbv h^{-1}), including the horizontal and vertical transport, dry deposition and the atmospheric mixing (Liu et al., 2022). To correct the effects of NO titration to O_3, we have replaced O_3 with O_X (=O_3+NO_2) during the calculation in this study (Pan et al., 2015).

2.3.3 Model performance

In order to judge the reliability of the model simulation, we calculated the index of agreement (IOA) based on the measured and modelled $P(O_3)_{net}$ and O_3 at 5 m above the ground level using the following equation (Liu et al., 2019):

$$IOA = 1 - \frac{\sum_{i=1}^{n}(O_i - S_i)^2}{\sum_{i=1}^{n}(|O_i - \bar{O}| - |S_i - \bar{O}|)^2} \tag{6}$$

Where S_i and O_i represents the simulated and observed $P(O_3)_{net}$ or O_3 values at the same time, respectively, $\bar{O}$ is the averaged observed value, and n is the data number. Furthermore, we also judged the model simulation performance using statistical measures, including the normalized mean bias (NMB) and normalized mean error (NME), which are defined as:

$$NMB = \frac{\sum_{i=1}^{n}(S_i - O_i)}{\sum_{i=1}^{n} O_i} \cdot 100\% \tag{7}$$

$$NME = \frac{\sum_{i=1}^{n}|S_i - O_i|}{\sum_{i=1}^{n} O_i} \cdot 100\% \tag{8}$$

Where S_i and O_i have the same meaning as Eq. (6), and n is the total number of such data pairs of interest. The results will be discussed in Sect. 3.2.2.

2.3.4 OH reactivity

In order to investigate the influence of the photochemical reactions of different VOCs to photochemical O_3 formation, we calculated the OH reactivities of different VOCs, which is the sum of concentrations of OH reactants multiplied by their reaction rate coefficients, as shown below:

349 $$k_{OH} = k_i \times [VOCs]_i \qquad (9)$$

350   where k_{OH} represents the total OH reactivity of a group of VOCs species, k_i

351 represents the rate constants between OH radicals and different VOCs species i,

352 $[VOCs]_i$ represents the concentration of species i. In this study, we summarized the OH

353 reactivities of different kinds of VOCs groups together to investigate their influence on

354 the vertical gradient $P(O_3)_{net}$ in Sect. 3.2.3.

355   **2.3.5   O$_3$ formation potential**

356 The O$_3$ formation potential is calculated using the product of the VOCs concentration

357 and the maximum incremental reactivity (MIR) coefficient (dimensionless, gram of O$_3$

358 produced per gram of VOCs) (Carter et al., 2012):

359 $$OFP_i = \sum_i [VOC]_i \times MIR_i \qquad (10)$$

360   Where OFP_i is the O$_3$ formation potential of species i, $[VOC]_i$ is the mass

361 concentration or emission of species i, and MIR_i denotes the maximum increment

362 reactivity of species i (g O$_3$/g VOCs).

363   **2.3.6   O$_3$ formation regime**

364   The sensitivity of photochemical O$_3$ production to its precursors was diagnosed by

365 calculating the relative incremental reactivity (RIR) using the OBM-MCM model. RIR

366 is defined as the percent change in O$_3$ photochemical production per percent change in

367 the concentration of its single precursor/precursor group (Cardelino and Chameides,

368 1995). Therefore, the RIR for precursor (group) X can be expressed as:

369 $$RIR = \frac{\Delta P(O_3)/P(O_3)}{\Delta X/X} \qquad (11)$$

370   where the $\Delta X/X$ represent the percent change in different O$_3$ precursors or

371 precursor groups. We classified the measured VOCs into anthropogenic organic

372 compounds (AVOC), biogenic organic compounds (BVOC), and OVOC group, and

373 investigated the O$_3$ formation sensitivity to these different types of VOCs.

374   **3.   Results and discussions**

375   **3.1 Vertical and temporal profile of O$_3$ and its precursors**

376   **3.1.1 O$_3$ and its precursors at 5 m ground level**

377   Figure 1 shows the time series of the major trace gases, photolysis rate constants,

and meteorological parameters at 5 m ground-level during the observation period at SZMGT. Over the 1-month field observation period, a total of 3 O_3 pollution episodes (referred to episodes hereafter) and 2 non-O_3 pollution episodes (referred to non-episodes hereafter) were captured. O_3 pollution episodes were defined as the days during which the hourly average O_3 concentration at ground-level (5 m) exceed the Grade II standard (102 ppbv, GB 3095-2012, China; Ambient Air Quality Standards, 2012), while the remaining days were defined as non-episodes. Episode days (marked as gray columns in Fig. 1) included November 13-18 (episode I), November 26 (episode II), and December 7-9 (episode III), while the non-episode days included November 22-25 (non-episode I), November 26-27 and 30 (non-episode II). The corresponding daytime mean values (6:00-18:00 LT) during all episode days and non-episode days are shown in Table 1. During the daytime of episode days (episodes I, II, and III), the mean concentrations of O_3 were 70.1±28.6, 59.5±32.4, and 71.3±31.0, respectively. The mean T and RH were 22.3±2.5 °C and 56.2±14.5 % for episode I, 20.4±3.2 °C and 52.2±16.7 % for episode II, and 20.6±3.4 °C and 58.2±17.2 % for episode III. During non-episode days, the mean concentrations of O_3 were 45.3±16.2 and 63.7±21.3 ppbv for non-episode I and II, respectively. The corresponding mean T and RH were 18.4±4.3 °C and 69.5±15.4 % for non-episode I, and 21.3±2.7 °C and 51.8 ±13.7 % for non-episode II. These observations indicate that the T and RH during episode days were not significantly different from those during non-episode days. This phenomenon contrasts with previous studies in the PRD area, where O_3 pollution episodes were generally associated with high T and low RH (Mousavinezhad et al., 2021; Hong et al., 2022).
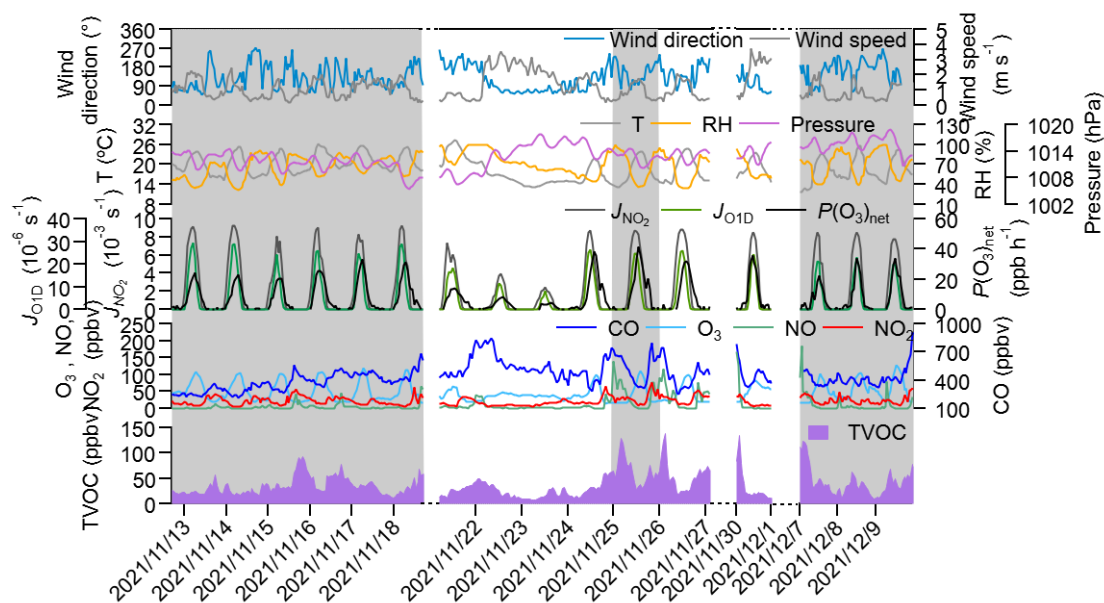
401

402 **Figure 1. Time series of major trace gases, photolysis rate constants, and meteorological**

403 **parameters at 5 m ground level during the observation period. The gray columns show the**

404 **typical O₃ episodes that occurred.**

405 **Table 1. Daytime major trace gases concentrations (units: ppbv), $P(O_3)_{net}$ (units: ppbv h⁻**
406 **¹), and meteorological parameters during different episodes and non-episodes during the**
407 **observation period (from 13 November to 9 December 2021) at SZMGT.**

Parameters	Mean±SD				
	Episode I	Episode II	Episode III	Non-episode I	Non-episode II
O_3	70.1±28.6	59.5±32.4	71.3±31.0	45.3±16.2	63.7±21.3
TVOC	29.6±10.6	53.8±21.7	42.9±11.5	23.3±8.6	26.8±11.1
CO	344.9±85.1	408.8±85.4	397.2±42.1	508.5±117.2	383.4±74.6
NO	2.3±2.6	13.1±17.4	6.6±13.8	2.9±2.0	6.8±13.1
NO_2	15.6±7.5	22.3±10.2	20.0±8.3	14.1±6.8	15.4±8.8
OFP (g m⁻³)	5.1E-4± 7.5E-5	1.0E-3± 2.0E-4	7.2E-4± 8.3E-5	4.1E-4± 5.6E-5	4.7E-4± 7.8E-5
$P(O_3)_{net}$* ppbv h⁻¹)	14.3±10.7	21.5±14.9	14.6±11.9	5.6±4.6	18.9±13.9
T (℃)	22.3±2.5	20.4±3.2	20.6±3.4	18.4±4.3	21.3±2.7
RH (%)	56.2±14.5	52.2±16.7	58.2±17.2	69.5±15.4	51.8±13.7
Wind speed (m s⁻¹)	1.3±0.5	1.2±0.4	1.1±0.5	1.8±0.9	2.1±0.9
wind direction (°)	115.5±48.7	128.6±35.3	144.8±57.1	115.0±57.6	115.3±36.2

408   * All values here were calculated as the mean average values during daytime (6:00-18:00 LT).

409   The mean concentrations of O₃ precursors, including CO, NO, NO₂, and the total

410   VOCs measured by PTR-TOF-MS (shown as TVOC in Fig. 1 and Table 1), did not

411   exhibit notable discrepancies between episodes and non-episodes. This suggests that

412   their concentrations during O_3 pollution episodes can vary, being either higher or lower

413   than those observed during non-episodes (as shown in Table 1). For example, through

414   there are days with very high hourly average O_3 concentrations which define O_3

415   pollution episodes-where levels exceed the Grade II standard of 102 ppbv-the

416   overall average O_3 concentrations for episode II is not higher than that of non-episode

417   II. This suggests that despite the occurrence of peak hourly levels, the average

418   concentration for episode II remains lower, highlighting the fluctuating pattern of

419   O_3 levels during these episodes. Further comparison of the daytime mean O_3

420   formation potential (OFP) and the measured $P(O_3)_{net}$ during episodes and non-episodes

421   showed no significant differences, ranging from 5.1×10^{-4} to 1.0×10^{-3} g m^{-3} and 14.3 to

422   21.5 ppb h^{-1}, respectively, during non-episodes, whereas they are ranged from $4.1 \times 10^{-}$

423   ^{4} to 4.7×10^{-4} g m^{-3} and 5.6 to 18.9 ppb h^{-1} respectively, during episodes. Although OFP

424   was always higher during episodes than during non-episodes, the mean $P(O_3)_{net}$ values

425   during episodes I and III were even lower than during non-episodes II. The higher O_3

426   concentrations may be due to the more stable weather conditions during episodes I and

427   III (with lower wind speed), which benefits the accumulation of O_3 formed by local

428   photochemical O_3 formation. While for non-episode II, even it processes higher $P(O_3)_{net,}$

429   the outflow of O_3 from the observation site by physical processes may be higher due to

430   the higher wind speed. These findings indicate that the O_3 pollution episodes stem from

431   either substantially elevated local photochemical O_3 formation (i.e., episode II), or the

432   accumulation of O_3 formed by moderate local photochemical O_3 formation under stable

433   weather conditions (i.e., episodes I and II). Notably, when local photochemical

434   reactions contribute intensely to the formation of O_3, favorable weather conditions

435   facilitating O_3 outflow diminish the likelihood of O_3 pollution occurrences (i.e., non-

436   episode II). These results indicate that O_3 pollution episodes are jointly affected by the

437   photochemical reactions and physical transport processes, which we will discuss in

438   more detail in Sect. 3.2.1.

439

440
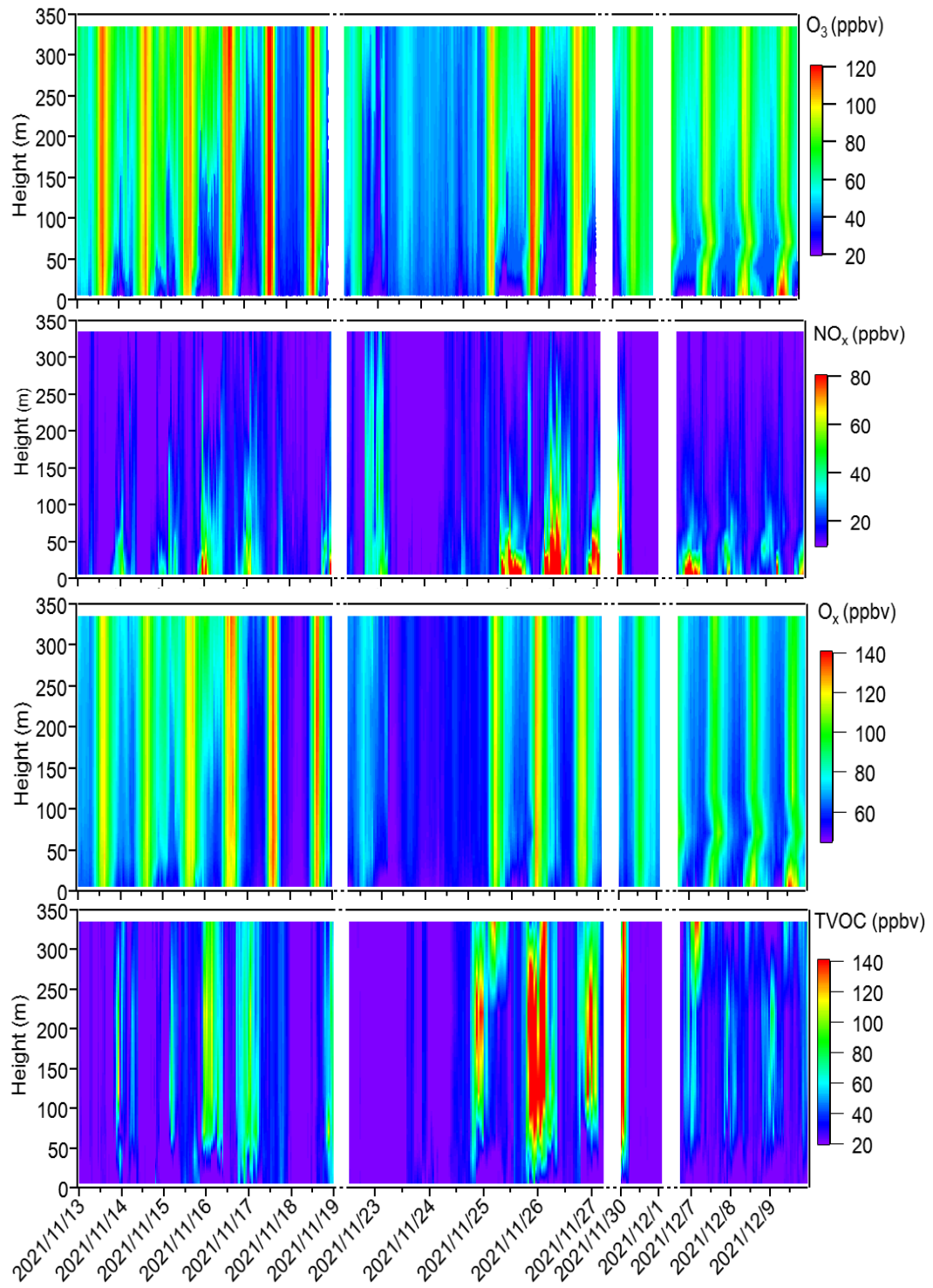
Figure 2. Time series of vertical profiles for O₃, NOx, Ox, and TVOC during the observation period. The contour plots are made using the measured values from six heights.

443

444
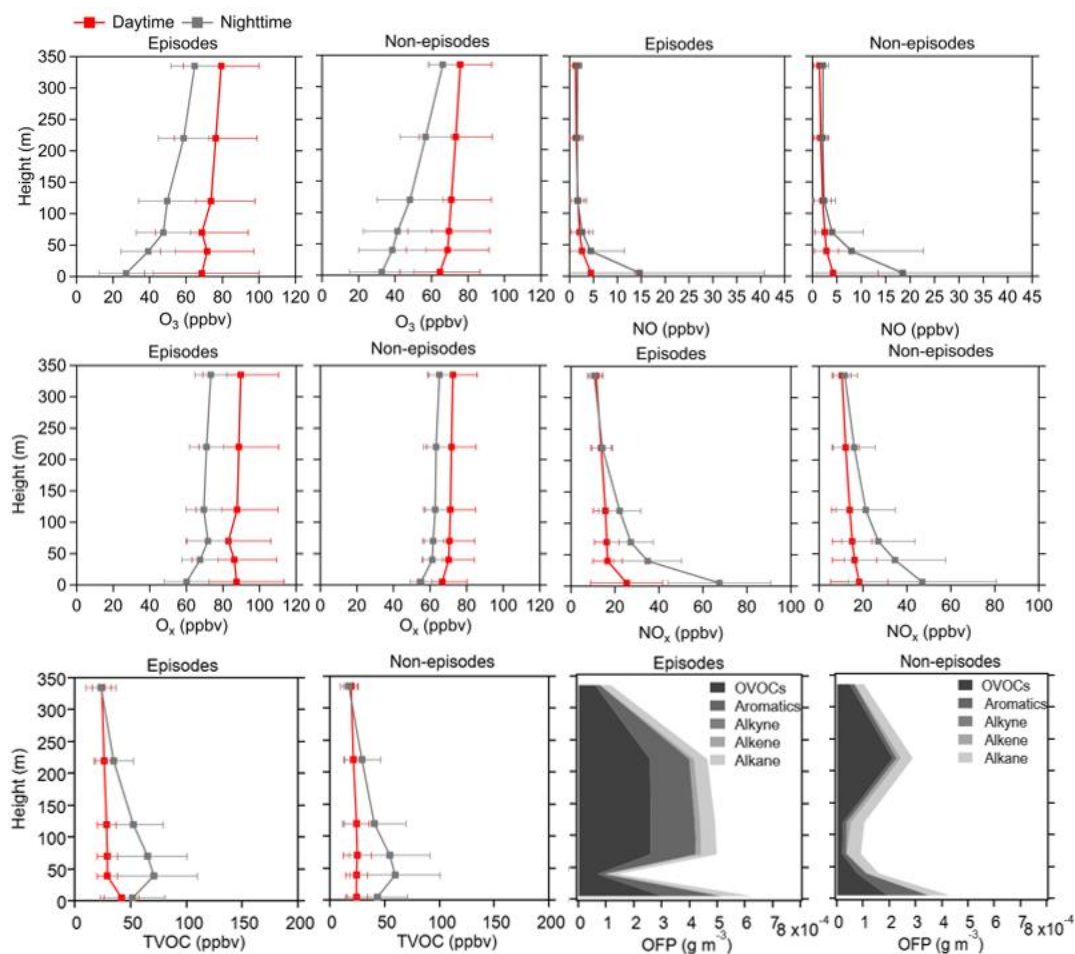
Figure 3. Average vertical profiles of O_3, NO, Ox, NOx, and TVOC during both daytime
and nighttime, and OFP of different VOCs types during daytime at six heights (5, 40, 70, 120,
220, and 335 m), including episodes and non-episodes throughout the observation period. The
error bars indicate the standard deviation calculated from the measured values during these
periods.

3.1.2 Vertical profiles of O_3 and its precursors at 5-335 m level

Figure 2 shows the contour plots illustrating the vertical profiles of O_3, NOx, Ox($=O_3+NO_2$), and TVOC. From Fig. 2, minimal vertical gradients were observed during daytime in the concentration of all species–O_3, NOx, Ox, and TVOC–due to the rapid vertical mixing effects. However, distinct vertical gradients were observed during nighttime owing to the stability of the nocturnal residual layer. Elevated concentrations of O_3 and Ox were identified at higher altitudes, whereas higher NOx concentrations predominantly occurred at ground level. We further elucidated the vertical distribution patterns of different pollutants as well as the OFP of different VOCs groups during local daytime (6:00-18:00 LT) and nighttime (19:00-5:00 LT) for both episodes and non-episodes, as shown in Fig. 3.

461   The vertical profiles of averaged concentrations of various pollutants exhibit
462   similar trends during both episodes and non-episodes, with O_3 showing an increasing
463   trend from 5 m above ground level to 355 m, aligning with findings from previous
464   studies (Zhang et al., 2019; Wang et al., 2021). Given that NOx has a significant
465   titration effect on O_3, the lower O_3 concentration at ground level may be attributed to
466   the increase in NOx concentration (Zhang et al., 2022) and also the dry deposition near
467   the ground (Li et al., 2022). NO and NOx showed an opposite trend compared to O_3.
468   These two factors jointly effected the Ox changing trend with heights, and consequently,
469   the gradients of Ox concentrations showed a weaker increasing trend from the 5 m
470   ground level to 355 m height compared to O_3. This observation demonstrated a more
471   pronounced NO titration effect at the 5 m ground level compared to the effect at 355 m
472   height. However, the TVOC showed variable trends with increased height for daytime
473   and nighttime during episodes and non-episodes. During daytime, TVOC initially
474   decreased from 5 m to 40 m, and then continuously increased from 40 m to 355 m
475   during episodes, while continuously slightly decreased from 5 m to 335 m during non-
476   episodes. During nighttime, TVOC concentrations first increased from 5 m to 40 m and
477   then continuously decreased from 40 m to 335 m during both episodes and non-episodes.
478   We further plotted the OFP of different VOCs groups at various altitudes, and found
479   that the total OFP was highest at 5 m ground level and exhibited higher levels during
480   episodes compared to non-episode periods. Subsequently, there was a significant
481   decrease at 40 m height during both episodes and non-episodes. However, there was a
482   sharp increase observed at 70 m, 120 m, and 220 m during episodes, contrasting with a
483   gradual rise during non-episode periods, which eventually reach a peak at 220 m during
484   non-episodes. A consistent decrease of OFP from 220 m to 335 m was observed during
485   both episodes and non-episodes. The OFP was primarily attributed to OVOCs at
486   different altitudes throughout both episodes and non-episodes, followed by aromatics
487   and alkane during episodes and non-episodes, respectively.

488   In conclusion, our daytime observations revealed minimal vertical gradients in the
489   concentrations of O_3, NOx, Ox, and TVOC, attributed to the rapid vertical mixing
490   effects driven by surface heating effects (Tang et al., 2017). This suggests that ground-
491   level O_3 concentrations would be representative of the entire vertical column.
492   Nonetheless, the OFP varies for different VOCs profiles at various heights, and the
493   vertical mixing effects facilitates the downward transport of O_3 photochemically

formed from higher altitudes to the near-ground layer. Consequently, a box model constraining to ground-level NOx and VOCs concentrations may not accurately reflect the in situ O_3 production in the vertical atmospheric column.

3.2 O_3 pollution episodes formation mechanism at near-ground surface

In this section, we first explored the possible reason for O_3 pollution episodes on the 5 m ground level, aiming to identify the contribution of chemical and physical processes to change in O_3 concentrations (Sect. 3.2.1). Subsequently, we assessed the modelling performance and investigated the potential reasons for the modelling bias in photochemical O_3 formation by comparing the measured $P(O_3)_{net}$ with the modelled $P(O_3)_{net}$ (Sect. 3.2.2). To gain insights into the photochemical O_3 formation mechanism at different heights and understand their role in overall O_3 pollution, we further discussed the chemical budget of O_3 at different heights (Sect. 3.2.3), the vertical and temporal variability of $P(O_3)_{net}$ and O_3 formation regime (Sect. 3.2.4), along with potential bias within the modelling approach (Sect. 3.2.5).

3.2.1   Contribution of chemical and physical processes to O_3 changes on the ground level

As concluded in Sect. 3.1.1, O_3 pollution episodes may be jointly affected by the photochemical reactions and physical transport. In order to identify the main reasons for O_3 pollution on the ground level, we calculated the contribution of chemical and physical processes to O_X concentration changes at 5 m ground level separately for all 3 episodes and 2 non-episodes. Typically, as dry deposition contributes a relatively small portion and can often be considered negligible, making vertical and horizontal transport the main contributors to physical processes (Tan et al., 2019).
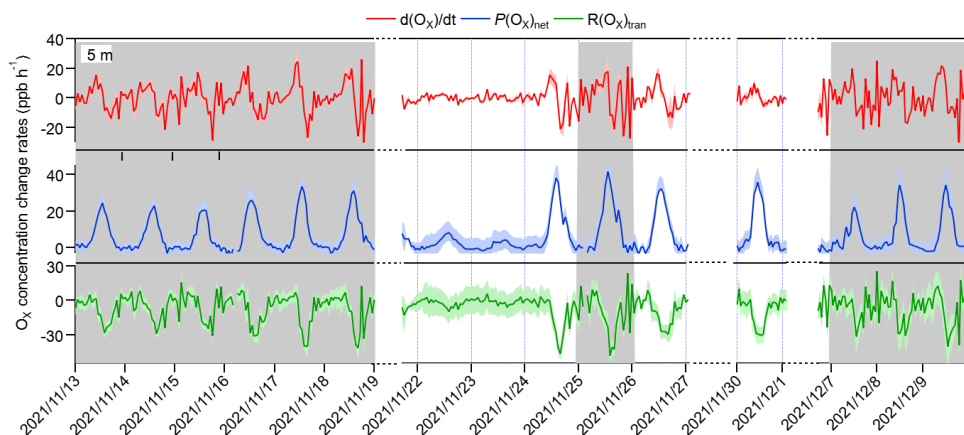
Figure 4. Time series of O_X concentration changes ($d(O_X)/dt$) and contributions from local photochemical production ($P(O_X)_{net}$) and physical transport ($R(O_X)_{tran}$). The shaded areas of $d(O_X)/dt$, $P(O_X)_{net}$, and $R(O_X)_{tran}$ represent one standard deviation (denoted by σ) of the mean $d(O_X)/dt$, the uncertainty of measured $P(O_X)_{net}$, and the propagated error of $R(O_X)_{tran}$, respectively.
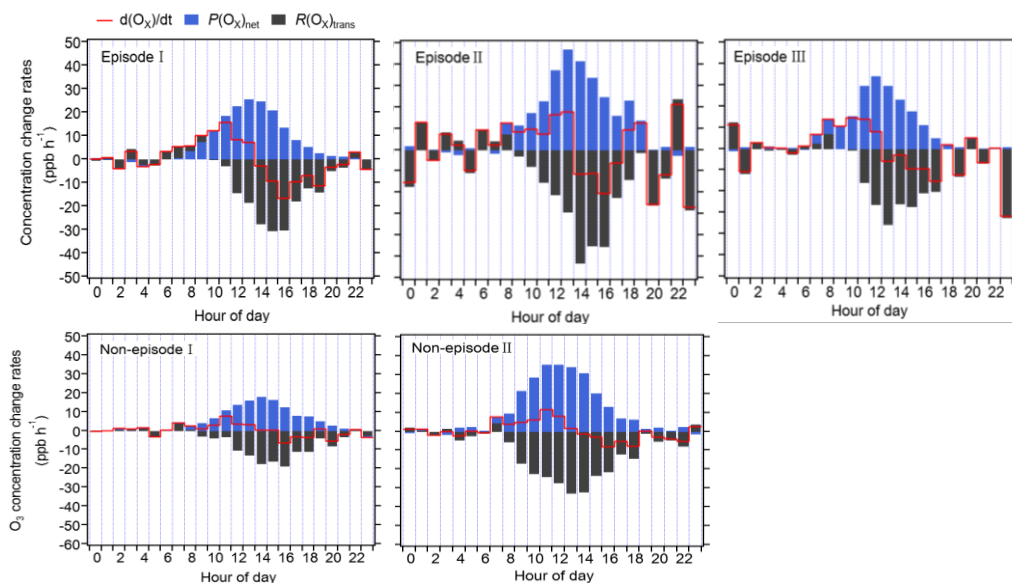
Figure 5. Diurnal variation of the contribution of chemical and physical transport to O_3 changes on the ground level.

$R(O_X)_{trans}$ at 5 m ground level was derived from $\frac{dO_X}{dt}$ manus $P(Ox)_{net}$, according to Eq. (5) shown Sect. 2.3.2, their hourly averages and diurnal variations are shown in Figs. 4 and 5, respectively. From these figures, it is evident that the fluctuation of the O_X concentration change rate ($d(O_X)/dt$) at ground level is typically small and primarily dominated by the physical processes during nighttime. During nighttime, $P(O_X)_{net}$ should be zero without sun radiation, the significant $P(O_X)_{net}$ shown in Fig. 5 may be

533 due to the measurement uncertainty of $P(O_X)_{net}$, which is determined by the
534 measurement error of O_X of CAPS-NO_2 monitor and the error caused by the light-
535 enhanced loss of O_3 in the reaction and reference chambers (as discussed in Sect. S4).
536 The measurement uncertainty of $P(O_X)_{net}$ is higher at lower $P(O_X)_{net}$ values (as shown
537 in Fig. 4), which was mainly determined by the instrumental error of O_X measurement
538 and the ambient O_X concentrations during nighttime. It was estimated to be ~ 38 % and
539 can be considered as the measurement precision. Around 6:00-7:00 LT, O_3
540 concentrations increase for all episodes and non-episodes, mainly due to physical
541 transport during episodes I and II and non-episodes I, while photochemical reactions
542 and physical processes are equally important for episodes III and non-episode II. This
543 could be due to short-term strong vertical turbulence in the early morning, which leads
544 to an expansion of the boundary layer height and makes the residual layer "leaky",
545 allowing vertical transport. At the same time, O_3 precursors were also transported down
546 from the residual layer, and with increasing sunlight, these O_3 precursors underwent
547 rapid photochemical reactions that competed with the physical processes between 6:00-
548 7:00 LT, leading to a sharp increase in $P(O_X)_{net}$ between 8:00 to 12:00 LT. The $P(O_X)_{net}$
549 peaked around 11:00-14:00 LT and started to decrease around 15:00, eventually
550 approaching zero by around 19:00-20:00 LT. Between 7:00-8:00 LT, $R(O_X)_{tran}>0$ for
551 all episodes and non-episodes, indicating inflow of O_3 from physical transport,
552 increasing surface O_3 concentration by averages of 4.7, 3.9, 2.3, 3.5, and 4.5 ppbv h^{-1}
553 for episodes I, II, III, and non-episodes I and II, respectively. From 9:00 to 10:00 LT,
554 $R(O_X)_{tran}>0$ only for episodes I, increasing the O_3 concentration by 1.5 ppbv h^{-1},
555 indicating inflow of O_3 from physical transport; on the contrary, $R(O_X)_{tran}<0$ for
556 episodes II and III, and non-episodes I and II, indicating outflow of O_3 from physical
557 transport, decreasing the O_3 concentration by 3.1, 0.1, 3.0, and 16.9 ppbv h^{-1},
558 respectively. After 10:00 LT, $R(O_X)_{tran}<0$ for all episodes and non-episodes, indicating
559 outflow of O_3 from the observation sites, possibly due to accumulated photochemically
560 formed O_3 increasing the concentration at the observation site, diffusing upward or to
561 surrounding areas.

562   In conclusion, the observed daytime O_3 concentration changes during all episodes
563 and non-episodes were influenced by both photochemical production and physical
564 transport. In the early morning, the increase in O_3 concentrations can be attributed to
565 photochemical reactions, physical processes, and possibly reduced NO titration effects

566   as the boundary layer height increases. Around noon, O_3 concentrations stabilize,

567   suggesting a balance between photochemical reactions and physical transport affecting

568   O_3 concentration changes. In the afternoon, O_3 concentrations decrease due to the

569   transport of photochemically formed O_3 from the observation site to upward directions

570   or the surrounding areas. Our findings indicate that local photochemical reactions

571   dominate O_3 pollution. For example, O_3 pollution episodes recorded during the

572   observation period manifest under specific conditions: ① high photochemical O_3

573   production (i.e., episode II); ② moderate photochemical O_3 productions coupled with

574   O_3 accumulation under stable weather conditions (i.e., episodes I and III). In contrast,

575   non-episodes observed during the observation period occur under different conditions:

576   ① low levels of photochemical O_3 production (i.e., non-episodes I); ② elevated

577   photochemical O_3 production, with O_3 transport to surrounding areas under favorable

578   diffusion conditions (i.e., non-episodes II).

3.2.2   The model performance

580   In order to test the simulation ability of OBM-MCM model for $P(O_3)_{net}$, we

581   compared the measured and modelled $P(O_3)_{net}$ at 5 m ground level, as depicted in Fig.

582   S3a. The measured and modelled $P(O_3)_{net}$ revealed close alignment during episodes I

583   and III, yet displayed discernible variations during episode II, non-episode I, and non-

584   episode II. Assessment metrics including IOA, NMB, and NME were computed based

585   on the observed and modelled $P(O_3)_{net}$ over the entire measurement period (as described

586   in Sect. 2.3.3). The IOA ranged between 0.87 (25th percentile) and 0.90 (75th percentile)

587   for the measured and modelled $P(O_3)_{net}$ across the measurement period, indicating the

588   acceptable performance of the OBM-MCM model simulation (a higher IOA value

589   signifies a stronger agreement between simulated and observed values). Additionally,

590   comparison of measured and modelled O_3 concentrations at different heights (as shown

591   in Fig. S4) revealed generally higher modelled values during daytime and closer

592   alignment during nighttime at lower heights (i.e., 5 m, 40 m, and 70 m), while

593   discrepancies were observed at higher heights (i.e., 120 m, 220 m, and 335 m). These

594   phenomena may be primarily attributed to uncertainties in assumed physical processes

595   in the modelling, such as vertical and horizontal transport. Previous studies have

596   utilized the comparison of measured and modelled O_3 concentrations to determine the

597   dilution factor in modelling studies, discovering that suitable dilution factors vary by

598   location (Yang et al., 2021). To achieve the best agreement between the modelled O_3

599 concentrations and the observed values, we applied different dilution factors (the

600 lifetime of the species) in the modelling, varying from 6 h to 24 h. We found that the

601 simulated O_3 is closest to the measured O_3 concentrations when the lifetime of the

602 species is set to 12 h. However, given that O_3 concentrations are affected by physical

603 transport processes, the dilution factor might only represent the outflow of O_3 from the

604 observation site. Therefore, there may be limitations in using this method for precise

605 comparisons. We further compared the measured and modelled $P(O_3)_{net}$ under

606 different dilution factors. The modelled $P(O_3)_{net}$ initially increases and then decreases

607 as the dilution factor decreases (equivalent to an increase of species lifetime). However,

608 the influence of varying dilution rates on the modelled $P(O_3)_{net}$ is minimal, constituting

609 less than 30 %, due to the short lifetimes of the HO_2 and RO_2 radicals, which determine

610 the $P(O_3)_{net}$ values (Wang et al., 2021). Notably, the modelled $P(O_3)_{net}$ closely matched

611 the measured values when the species lifetime was set to 12 h, as illustrated in Fig. S3b.

612 Consequently, a constant dilution factor of $1/43200$ s^{-1} was applied throughout the

613 observation period. Further investigations revealed an IOA range between 0.80 (25th

614 percentile) and 0.82 (75th percentile) for measured and modelled O_3 concentrations at

615 5 m ground level, which lies in between the IOA result for the modelled and observed

616 O_3 concentrations in previous studies, which range between 0.68 and 0.89 (Wang et al.,

617 2018), signifying the modelling results for O_3 concentrations here are acceptable. The

618 calculated NMB and NME using the modelled and observed $P(O_3)_{net}$ at 5 m ground

619 level during the whole measurement period ranged from -0.42 (25th percentile) to -0.31

620 (75th percentile) and -0.42 (25th percentile) to 0.54 (75th percentile), respectively. These

621 analysis results indicate that the model underestimates the measured $P(O_3)_{net}$ by a factor

622 ranging from 1.42 (25th percentile) to 1.31 (75th percentile), calculated as (1+|NMB|),

623 and the simulation results are reliable (with -1<NME<1).

624   The mean diel variation of measured and modelled $P(O_3)_{net}$ during different

625 episodes and non-episodes are shown in Fig. 6a-e. The maximum daily $P(O_3)_{net}$ values

626 were 29.3, 47.2, and 34.2 ppbv h^{-1} for episodes I, II, and III, and 17.9 and 35.5 ppbv h^{-1}

627 ^{1} for non-episodes I and II, respectively. These values were comparable to or lower than

628 those measured in urban areas of Houston, United States (40-50 and 100 ppbv h^{-1} in

629 autumn and spring, respectively) (Baier et al., 2015; Ren et al., 2013), but higher than

630 those measured in a remote area of Japan (10.5 ppbv h^{-1} in summer) and an urban area

631 of Pennsyvania, United States (~ 8 ppbv h^{-1} in summer) (Sadanaga et al., 2017; Cazorla

and Brune, 2020). The averaged diel profiles of measured and simulated $P(O_3)_{net}$ exhibited large standard deviations (as depicted in Table 1), representing their day-to-day variation throughout the campaign. The measured $P(O_3)_{net}$ were mostly higher than the modelled $P(O_3)_{net}$, which could be attributed to the underestimation of RO_2 under high NO conditions, leading to substantial disparities between calculated $P(O_3)_{net}$ derived from measured and modelled RO_2 concentrations, as highlighted in previous studies (Whalley et al., 2018, 2021; Tan et al., 2017, 2018). The median value of [measured $P(O_3)_{net}$-modelled $P(O_3)_{net}$]/measured $P(O_3)_{net}$ ranged from 22% to 45% for different episodes and non-episodes. To delve deeper, we further investigated the relationship between the daily disparities of measured and modelled $P(O_3)_{net}$ ($\Delta P(O_3)_{net}$ = measured $P(O_3)_{net}$-modelled $P(O_3)_{net}$) and average daytime NO concentrations during different episodes and non-episodes, as depicted in Fig. 6f. The observed elevated $\Delta P(O_3)_{net}$ at higher NO concentrations aligns with findings from previous studies, which suggest that multiple factors could contribute to these outcomes. For example, the reaction of OH with unknown VOCs (Tan et al., 2017), the lack of correction for the decomposition of $CH_3O_2NO_2$, the missing RO_2 production from photolysis $ClNO_2$ (Whalley et al., 2018; Tan et al., 2017), and the underestimation of OVOCs photolysis (Wang et al., 2022b) in modelling approaches may lead to the underestimation of RO_2, thus underestimating the modelled $P(O_3)_{net}$. Further analysis showed that the underestimation of $P(O_3)_{net}$ can lead to the NOx-limited regime being shifted to the VOCs-limited regime, thus underestimating the NOx-limited regime (Wang et al., 2022b, 2024). However, the derived IOA, NMB, and NME values from the modelled and observed $P(O_3)_{net}$ (and O_3) at 5 m ground during different episodes and non-episodes indicate that the model proficiently reproduces the genuine $P(O_3)_{net}$ at the observation site (as shown in Table S3). Consequently, these results provide confidence in exploring the vertical and temporal variations of $P(O_3)_{net}$ and O_3 formation sensitivities utilizing the outcomes from the modelling approach. Nonetheless, it is important to acknowledge and discuss the potential biases caused by the modelling methodology in this study.
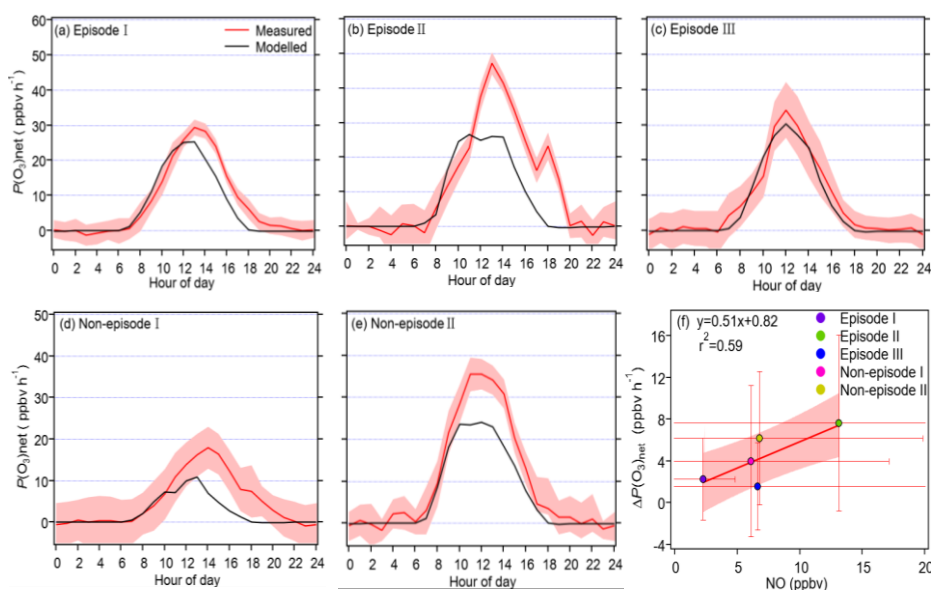
Figure 6. (a-e) diurnal variations of the measured and modelled $P(O_3)_{net}$ during the observation period, and (f) the relationship between the average daily differences of measured and modelled $P(O_3)_{net}$ ($\Delta P(O_3)_{net}$) and the average daytime NO concentrations during different episodes and non-episodes.

3.2.3 Vertical and temporal variability of $P(O_3)_{net}$ budget

The detailed $P(O_3)_{net}$ budget at different heights during the observation period from the modelling results are shown in Fig. 7. Across various heights and different episodes and non-episodes, the contributions of different reaction pathways to $P(O_3)$ were almost the same, with HO_2+NO as the major O_3 production pathway, followed by CH_3O_2+NO and other RO_2+NO, where other RO_2+NO encompasses all RO_2 except CH_3O_2. This result aligns with previous studies (Liu et al., 2021; Liu et al., 2022). The major O_3 destruction pathway was $OH+NO_2$ (loss of OH radicals), followed by net RO_2+NO_2 (form peroxyacetyl nitrate, commonly called PAN species) and O_3 photolysis, while other O_3 destruction pathways, including O_3+OH, O_3+HO_2, $C_5H_8+O_3$, $C_3H_6+O_3$, and $C_2H_4+O_3$, together contributed negligibly to O_3 destruction. These $P(O_3)$ and $D(O_3)$ reaction pathways occurred between 6:00-18:00 LT, exhibiting strong diurnal variation characterized by a sharp increase between 6:00-11:00 LT in the morning, peaking between 11:00 and 14:00 LT, and decreasing rapidly after 14:00 LT. These phenomena were in accordance with the concentration changes of the major oxidants (i.e., OH, O_3, and NO_3), as shown in Fig. S5, where OH radicals and O_3 concentrations increased significantly in the morning and reached a peak around noon, followed by sharp afternoon decreases.

687   The diurnal changes in the concentrations of different reaction pathways to $P(O_3)$

688   and $D(O_3)$ at 5 m ground level during different episodes and non-episodes are depicted

689   in Fig. S6. We note that the maximum total $P(O_3)$ resulting from diel variations at 5 m

690   ground level for episode I, II, and III were 32.0, 34.9, and 38.3 ppbv h^{-1}, respectively.

691   These values were consistently higher than the maximum total $P(O_3)$ observed for non-

692   episodes I and II, which were 15.6 and 30.7 ppbv h^{-1}, respectively. However, as $P(O_3)_{net}$

693   was determined by both $P(O_3)$ and $D(O_3)$, the maximum total $D(O_3)$ values resulting

694   from diel variations during episodes I, II, III, and non-episode I, II, were 5.0, 5.7, 5.1,

695   2.4, and 5.3 ppbv h^{-1}, respectively. Consequently, the modelled $P(O_3)_{net}$ during episodes

696   does not exhibiting a statistically significant difference from that during non-episodes

697   (Mann-Whitney p value=0.12), as shown in Fig. S5, which is in agreement with the

698   measured $P(O_3)_{net}$ (Mann-Whitney p-value=0.28), as depicted in Sect. 3.1.1.

699   The diurnal variation of $P(O_3)_{net}$ during different episodes and non-episodes

700   obtained by OBM-MCM modelling at different heights are shown in Fig. 8. We saw

701   that the $P(O_3)_{net}$ all showed a decreasing trend with the increase of the measurement

702   height during different episodes and non-episodes, but the variation of $P(O_3)_{net}$ along

703   with the measurement height differed for different episodes and non-episodes. For

704   example, the decrement of the averaged $P(O_3)_{net}$ during 6:00-18:00 LT from 5 m to 335

705   m were 1.5 and 0.6 ppbv h^{-1} for episode I and non-episode I, respectively, which was

706   relatively smaller than that during episode II, episode III, and non-episode II, which

707   were 5.3, 5.4, and 4.0 ppbv h^{-1}, respectively. To explore the reason, we plotted the

708   differences of calculated OH reactivities at 5 m and 335 m of different VOCs groups

709   (marked as ΔOH reactivity) as a function of the $P(O_3)_{net}$ change at 5 m and 335 m

710   (marked as $\Delta P(O_3)_{net}$), including nonmethane hydrocarbons (NMHC), anthropogenic

711   volatile organic compounds (AVOC), biogenic volatile organic compounds (BVOC),

712   and oxygenated volatile organic compounds (OVOC) (as shown in Fig.8f). The VOCs

713   species included in each category are listed in Table S2. We found that the OH

714   reactivities of AVOC and OVOC had the highest correlation coefficients (R^2) with the

715     $\Delta P(O_3)_{net}$, which are 0.85 and 0.67, respectively, indicating their predominant influence

716   on the decrement of $P(O_3)_{net}$ from 5 m to 335 m. However, the OH reactivity change

717   from 5 m to 335 m of different groups was quite different. Therefore, we further

718   explored O_3 formation sensitivity to its different VOCs precursors and precursor groups.

719
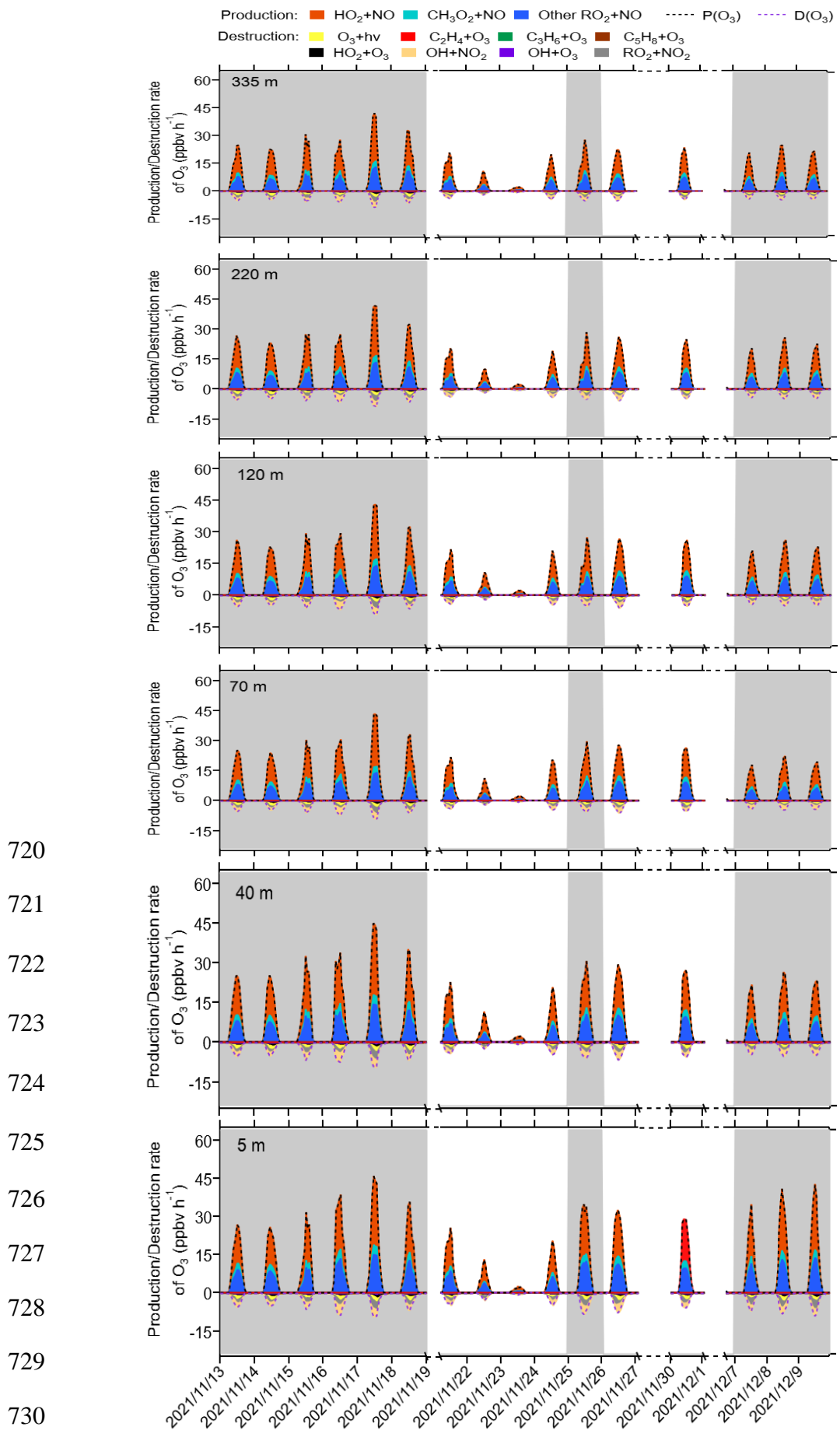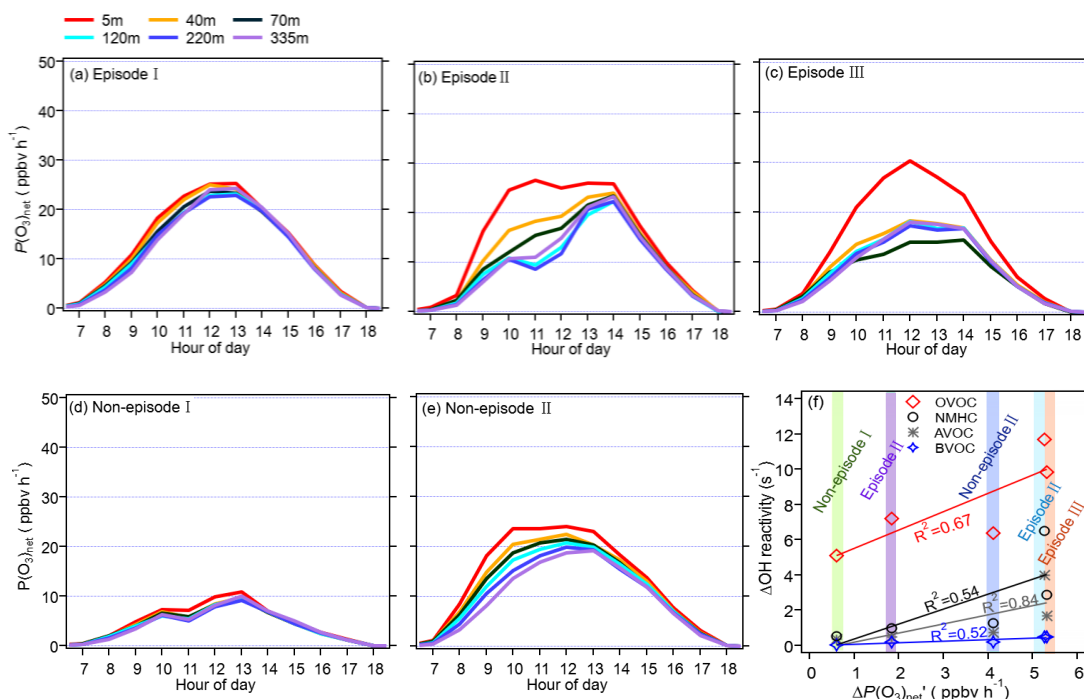
734

735   **Figure 8. (a-e) Diurnal variation of vertical profile of the model-simulated $P(O_3)_{net}$**

736   **during different episodes and non-episodes from 13 November to 9 December 2021, and (f)**

737   **the relationship between the average daytime differences of modelled $P(O_3)_{net}$ (denoted as**

738   **$\Delta P(O_3)_{net}$), and OH reactivity of different precursor groups at 5 m and 335 m (denoted as ΔOH**

739   **reactivity).**

740   **3.2.4   Vertical distributions of O$_3$ formation regime**

741   To investigate the reasons behind the variable distribution of $P(O_3)_{net}$ at varying

742   heights, we clarified the sensitivity of O$_3$ formation to different O$_3$ precursors or

743   precursor groups, including NMHC, AVOC, BVOC, OVOC, CO, and NOx, by

744   calculating their RIRs during different episodes and non-episodes, as shown in Fig. 9.

745   The VOCs species, categorized into different precursor groups as listed in Table S2,

746   indicate that some species depicted in Figure 9 may appear in multiple categories and

747   hence could be repeated. As illustrated in Fig. 9, the RIR values for different O$_3$-

748   precursors or precursor groups don't exhibit significant variation at different heights

749   during specific episodes or non-episodes, indicating a similar photochemical O$_3$

750   formation regime. However, the O$_3$ formation regimes differ between different episodes

751   or non-episodes. During O$_3$ polluted episode I, O$_3$ formation is located in a transition

regime and is more sensitive to VOCs emissions. Conversely, during O_3 polluted episodes II and III, and non-episodes I and II, it is located in VOCs sensitive regime. This finding aligns with previous studies suggesting that photochemical O_3 formation in the PRD region is likely VOC-limited or mixed-limited (Hong et al., 2022; Lu et al., 2018). The results suggest that the complexity of O_3 mitigation at the observation site. For example, during polluted episode I, reducing both VOCs and NOx can mitigate photochemical O_3 formation. However, during other O_3 polluted episodes and non-episodes, reducing VOCs can effectively alleviate photochemical O_3 formation, while reducing NOx might aggravate it. Nevertheless, during all episodes and non-episodes, O_3 formation is most sensitive to AVOC (RIR: 0.83-1.12), followed by OVOC (RIR: 0.59-0.79) at different heights, indicating the urgent need to reduce AVOC and OVOC emissions to mitigate O_3 pollution in this area.
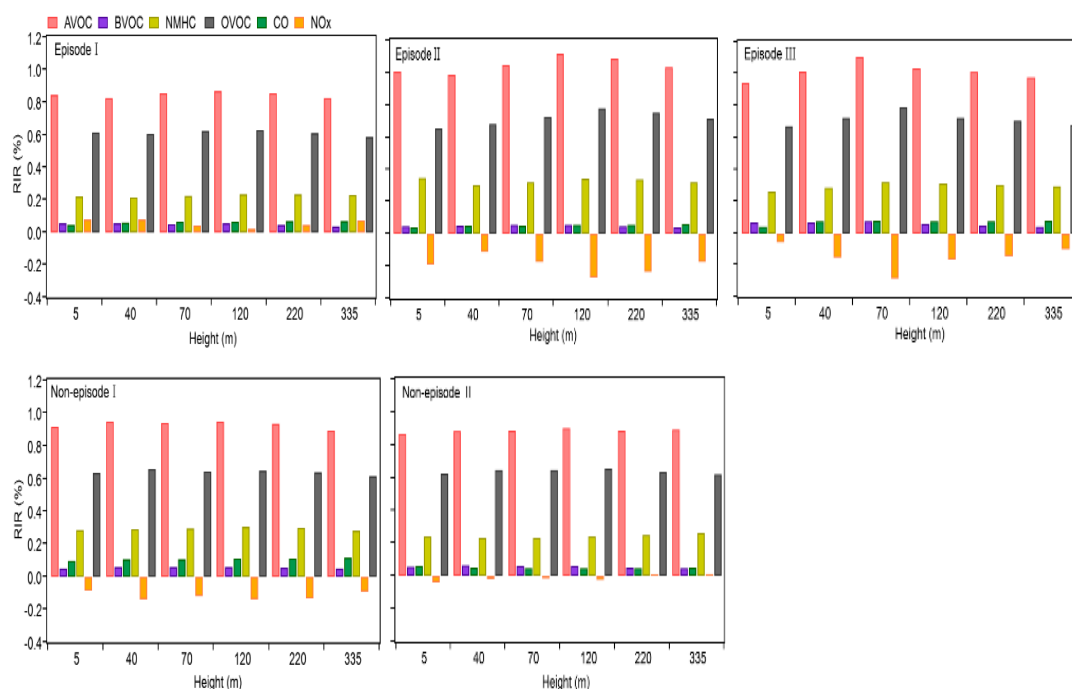
Figure 9. RIR values for O_3-precursor or precursor groups at different heights during different classified episodes.

The RIR tests for different episodes and non-episodes at various hours of the local daytime are illustrated in the Supplement (Fig. S7). The results indicate that the diurnal changes of RIR values for different episodes and non-episodes exhibit remarkable similarities. In the morning, the RIR values for various VOC groups, including AVOC, BVOC, OVOC, and CO, are typically higher than those for NOx. However, they gradually decrease throughout the day until 16:00 LT, then increase and reach a peak

773   at 18:00 LT. Interestingly, the RIR values at this peak are lower than those at 8:00 LT

774   in the morning. Conversely, the RIR values for NOx are usually around zero or below

775   zero during most of the day, gradually increasing around 16:00 LT and peaking at 18:00

776   LT. This suggests a transition in the photochemical O_3 formation regime throughout

777   the day, shifting from a VOC-limited regime in the morning to a transition regime and

778   more sensitive to NOx in the afternoon around 16:00 LT. The diurnal variations of the

779   RIRs of different O_3 precursors or precursor groups offer detailed insights into the

780   dominant factors influencing the photochemical formation of O_3 at different times of a

781   day.

782   Through the sensitivity study, NOx is not found to be the limiting factor affecting

783   $P(O_3)_{net}$, therefore, reactions involving NOx in the ROx radicals cycle, such as

784   $RO_2+NO \rightarrow HO_2$ and $HO_2+NO \rightarrow OH$, should occurred efficiently. Conversely,

785   reactions not involving NOx, such as $OH+VOCs \rightarrow RO_2$, should be the limiting steps of

786   the ROx radicals cycling. Given that photochemical O_3 formation is most sensitive to

787   AVOC and OVOC groups, we further identified and presented the three VOC species

788   with the highest OFP during different episodes and non-episodes in Table S4. Results

789   show that compounds such as toluene, *m/p*-xylene, and n-butane in AVOC group,

790   formaldehyde, hydroxyacetone, and ethanol in OVOC group have identified as the most

791   significant contributors to the total OFP in all episodes and non-episodes. Toluene, *m/p*-

792   xylene, and n-butane are often associated with specific industrial processes (Shi et al.,

793   2022; Liang et al., 2017), while formaldehyde, hydroxyacetone, and acetaldehyde can

794   originate from both the industrial processes and natural sources (Parrish et al., 2012;

795   Fan et al., 2021; Spaulding et al., 2003; Salthammer 2023). Priority of these emission

796   sources should be given to reducing AVOC and OVOC to mitigate O_3 pollution in the

797   PRD area of China.

4   Conclusions

799   We carried out a field observation campaign in an urban area in Pearl River Delta

800   (PRD) in China, focusing on investigating the vertical temporal variability of near-

801   surface O_3 production mechanisms by using a newly built vertical observation system

802   and the observation-based model coupled to the Master Chemical Mechanism (OBM-

803   MCM) v3.3.1. In total, three O_3 pollution episodes and two non-episodes occured

804   during the observation period. To assess the modelling performance for O_3 production

805   rates and sensitivity, as well as to investigate the potential reasons for O_3 pollution

806   episodes at 5 m ground level, a net photochemical O_3 production rate (NPOPR, $P(O_3)_{net}$)

807   detection system based on the current dual-channel reaction chamber technique was

808   employed to directly measure $P(O_3)_{net}$ at 5 m ground-level.

809   The vertical profiles of averaged concentrations of various pollutants exhibit

810   similar trends during both episodes and non-episodes. The O_3, NOx, and Ox

811   concentrations show minimal vertical gradient during the daytime due to rapid vertical

812   mixing effects, but distinct vertical gradients emerge during nighttime owing to the

813   stability of the nocturnal residual layer. Higher concentrations of O_3 and Ox were

814   observed at higher heights, while elevated NO and NOx concentrations were mainly

815   detected at ground level. Given that NO has a significant titration effect on O_3, the lower

816   O_3 concentration at ground level may be attributed to the increase in NOx concentration

817   due to a more pronounced NO titration effect, besides the dry deposition near the

818   ground. However, the TVOC and their OFP exhibited variable trends with increased

819   height during both daytime and nighttime, observed in episodes and non-episodes,

820   which indicates the complexities of O_3 formation mechanisms at different heights

821   throughout the atmospheric column. Total OFP was highest at the 5 m ground level and

822   exhibited higher levels during episodes compared to non-episode periods. The OFP was

823   primarily attributed to OVOCs at different altitudes throughout both episodes and non-

824   episodes.

825   The mean concentrations of O_3 precursors, including CO, NO, NO_2, and TVOC,

826   were not consistently elevated during episodes compared to their levels during non-

827   episodes. By considering the observed O_3 concentrations change and the measured

828    $P(O_3)_{net}$ at 5 m ground level, we found that the O_3 pollution episodes were influenced

829   by both photochemical production and physical transport, with local photochemical

830   reactions playing a key role. O_3 pollution episodes recorded during the observation

831   period occured under specific conditions: ① high photochemical O_3 productions; ②

832   moderate photochemical O_3 productions coupled with O_3 accumulation under stable

833   weather conditions. The index of agreement (IOA) ranged from 0.87 (25th percentile)

834   to 0.90 (75th percentile) for the measured and modelled $P(O_3)_{net}$ across the measurement

835   period, indicating the rationality to investigate the vertical and temporal variability of

836   O_3 formation mechanisms using modelling results. However, the measured $P(O_3)_{net}$

837   generally exceeded the modelled $P(O_3)_{net}$, the differences between measured and

838   modelled $P(O_3)_{net}$ ($\Delta P(O_3)_{net}$) were found to be correlated with NO concentrations. Base

839   on previous studies, this phenomenon could potentially be attributed to the

840   underestimation of RO_2 at high NO conditions, arising from inadequate knowledge

841   concerning photochemical reaction mechanisms. Therefore, the potential biases caused

842   by the modelling methodology were acknowledged and discussed.

843   From the modelling results, the contribution of different reaction pathways to $P(O_3)$

844   was almost the same at varying heights during both episodes and non-episodes, with

845   HO_2+NO as the major O_3 production pathway, followed by other RO_2+NO (comprising

846   all RO_2 except CH_3O_2) and CH_3O_2+NO. The major O_3 destruction pathway was

847    $OH+NO_2$ (loss of OH radicals), followed by net RO_2+NO_2 (forming peroxyacetyl

848   nitrate) and O_3 photolysis. However, other O_3 destruction pathways, including O_3+OH,

849   O_3+HO_2, $C_5H_8+O_3$, $C_3H_6+O_3$, and $C_2H_4+O_3$, collectively contributed negligibly to O_3

850   destruction. Nevertheless, $P(O_3)_{net}$ showed a decreasing trend with the increase of

851   height during different episodes and non-episodes, which was found mainly attributed

852   to the decline in O_3 precursor concentrations, specifically anthropogenic organic

853   compounds (AVOC) and oxygenated volatile organic compounds (OVOC) groups. We

854   observed that modelling biases were correlated with NO concentrations and VOCs

855   categories, impacting $P(O_3)_{net}$ through the regulation of the RO_2 radicals' budget. The

856   median relative difference between measured and modelled $P(O_3)_{net}$ ranged from 22-

857   45 % during different episodes and non-episodes. Therefore, the variation of $P(O_3)_{net}$

858   along with the measurement height might be even larger than our initial assessment.

859   Similar photochemical O_3 formation regimes were observed at different heights

860   during specific episodes or non-episodes, yet they varied between different episodes or

861   non-episodes. O_3 formation was predominantly located at a transition regime and more

862   sensitive to VOCs emissions during O_3-polluted episode I, whereas it shifted to a

863   VOCs-sensitive regime during O_3-polluted episodes II and III, as well as non-episodes

864   I and II. Further analysis revealed a daytime shift in the photochemical O_3 formation

865   regime, transitioning from a VOC-limited regime in the morning to a transition regime

866   more sensitive to NOx round 16:00 LT in the afternoon. However, the underestimation

867   of RO_2 radicals in the modelling, especially at lower heights with higher NO

868   concentrations, could result in an overestimate of the VOCs-limited regime. This study

869   highlights the need for more precise analysis using direct measurement techniques in

870   future studies. Nonetheless, throughout all episodes and non-episodes, O_3 formation is

871 most sensitive to AVOC, followed by OVOC at various heights, emphasizing the urgent

872 need to reduce emissions of these compounds to mitigate O_3 pollution in this area.

873 This is the first measurement report of the vertical-temporal of O_3 formation

874 mechanisms near the ground surface. Together with the deliberation of the possible bias

875 on the vertical-temporal profile of O_3 formation rate and sensitivity using modelling

876 studies, this research provides critical foundational insights. The findings provide us in-

877 depth understanding of near-ground vertical variability in O_3 formation mechanisms,

878 which are influenced by the concentrations of VOCs and NOx, and the distinct OFP

879 associated with different VOCs profiles. During daytime, the vertical mixing of air

880 masses is substantially enhanced due to the effect of surface heating. Consequently,

881 photochemically formed O_3 at higher altitudes can be vertically transported downward

882 to the near-ground layer. Under this condition, control strategies for O_3 precursors

883 based on the O_3 formation mechanisms on the ground-level are insufficient. A more

884 comprehensive approach is necessary to effectively address the complexities of O_3

885 production throughout the atmospheric column. The vertical variability of O_3

886 formation mechanisms should be taken into account when making effective O_3 control

887 strategies in the PRD area of China.

888 *Data availability.* Data related to this article are available online *at*

889 https://zenodo.org/records/10473104.

890 *Author contributions.* BY, JZ, XBL, and MS designed the experiment, YXH and

891 JZ performed the $P(O_3)_{net}$ measurement, BY and XBL built the vertical observation

892 system based on SZMGT. JZ, CZ, AL, BY, JPZ, YXH, YW, XBL, XJH, XS, YC, SY,

893 SY, YW, JPQ collected and analysed the data. JZ wrote the manuscript, all authors

894 revised the manuscript.

895 *Competing interests.* The authors declare that they have no known competing

896 interests.

897 *Acknowledgements.* This study was funded by the Key-Area Research and

898 Development Program of Guangdong Province (grant no. 2020B1111360003), the

899 National Natural Science Foundation of China (No. 42305096), and the Natural Science

900 Foundation of Guangdong Province (grant no. 2020A1515110526).

901 **References**

902   Anenberg, S. C., Schwartz, J., Shindell, D., Amann, M., Faluvegi, G., Klimont,
903 Z., Janssens-Maenhout, G., Pozzoli, L., Van Dingenen, R., Vignati, E., Emberson, L.,
904 Muller, N. Z., West, J. J., Williams, M., Demkine, V., Hicks, W. K., Kuylenstierna, J.,
905 Raes, F., and Ramanathan, V.: Global air quality and health co-benefits of mitigating
906 near-term climate change through methane and black carbon emission controls,
907 Environ. Health. Perspect., 120, 831-839, 10.1289/ehp.1104301, 2012.

908   Baier, B. C., Brune, W. H., Lefer, B. L., Miller, D. O., and Martins, D. K.: Direct
909 ozone production rate measurements and their use in assessing ozone source and
910 receptor regions for Houston in 2013, Atmos. Environ., 114, 83-91,
911 10.1016/j.atmosenv.2015.05.033, 2015.

912   Benish, S. E., He, H., Ren, X., Roberts, S. J., Salawitch, R. J., Li, Z., Wang, F.,
913 Wang, Y., Zhang, F., Shao, M., Lu, S., and Dickerson, R. R.: Measurement report:
914 Aircraft observations of ozone, nitrogen oxides, and volatile organic compounds over
915 Hebei Province, China, Atmos. Chem. Phys., 20, 14523-14545, 10.5194/acp-20-14523-
916 2020, 2020.

917   Carter, W. P. L. and Heo G. (2012): Development of Revised SAPRC Aromatics
918 Mechanisms, Report to the California Air Resources Board Contracts No. 07-730 and
919 08-326, April 12, 2012. Available at:
920 http://www.cert.ucr.edu/~carter/absts.htm#saprc11, 2012.

921   Cazorla, M. and Brune, W. H.: Measurement of ozone production sensor, Atmos.
922 Meas. Tech., 3, 545-555, 10.5194/amt-3-545-2010, 2010.

923   Decker, Z. C. J., Zarzana, K. J., Coggon, M., Min, K.-E., Pollack, I., Ryerson, T.
924 B., Peischl, J., Edwards, P., Dubé, W. P., Markovic, M. Z., Roberts, J. M., Veres, P. R.,
925 Graus, M., Warneke, C., de Gouw, J., Hatch, L. E., Barsanti, K. C., and Brown, S. S.:
926 Nighttime chemical transformation in biomass burning plumes: a box model analysis
927 initialized with aircraft observations, Environ. Sci. Technol., 53, 2529-2538,
928 10.1021/acs.est.8b05359, 2019.

929   Fan, J., Ju, T., Wang, Q., Gao, H., Huang, R., and Duan, J.: Spatiotemporal
930 variations and potential sources of tropospheric formaldehyde over eastern China based
931 on OMI satellite data, Atmos. Pollut. Res., 12, 272-285, 10.1016/j.apr.2020.09.011,
932 2021.

933   Fiore, A. M., Dentener, F. J., Wild, O., Cuvelier, C., Schultz, M. G., Hess, P.,
934 Textor, C., Schulz, M., Doherty, R. M., Horowitz, L. W., MacKenzie, I. A., Sanderson,
935 M. G., Shindell, D. T., Stevenson, D. S., Szopa, S., Van Dingenen, R., Zeng, G.,
936 Atherton, C., Bergmann, D., Bey, I., Carmichael, G., Collins, W. J., Duncan, B. N.,
937 Faluvegi, G., Folberth, G., Gauss, M., Gong, S., Hauglustaine, D., Holloway, T.,
938 Isaksen, I. S. A., Jacob, D. J., Jonson, J. E., Kaminski, J. W., Keating, T. J., Lupu, A.,
939 Marmer, E., Montanaro, V., Park, R. J., Pitari, G., Pringle, K. J., Pyle, J. A., Schroeder,
940 S., Vivanco, M. G., Wind, P., Wojcik, G., Wu, S., and Zuber, A.: Multimodel estimates
941 of intercontinental source-receptor relationships for ozone pollution, J. Geophys. Res.,
942 114, 10.1029/2008jd010816, 2009.

943   Geng, C., Wang, J., Yin, B., Zhao, R., Li, P., Yang, W., Xiao, Z., Li, S., Li, K.,
944 and Bai, Z.: Vertical distribution of volatile organic compounds conducted by tethered
945 balloon in the Beijing-Tianjin-Hebei region of China, J. Environ. Sci., 95, 121-129,
946 10.1016/j.jes.2020.03.026, 2020.

947   Hao, Y., Zhou, J., Zhou, J. P., Wang, Y., Yang, S., Huangfu, Y., Li, X. B., Zhang,
948 C., Liu, A., Wu, Y., Zhou, Y., Yang, S., Peng, Y., Qi, J., He, X., Song, X., Chen, Y.,
949 Yuan, B., and Shao, M.: Measuring and modeling investigation of the net
950 photochemical ozone production rate via an improved dual-channel reaction chamber
951 technique, Atmos. Chem. Phys., 23, 9891-9910, 10.5194/acp-23-9891-2023, 2023.

952   Hong, Q., Zhu, L., Xing, C., Hu, Q., Lin, H., Zhang, C., Zhao, C., Liu, T., Su, W.,
953 and Liu, C.: Inferring vertical variability and diurnal evolution of O_3 formation
954 sensitivity based on the vertical distribution of summertime HCHO and NO_2 in
955 Guangzhou, China, Sci. Total Environ., 827, 10.1016/j.scitotenv.2022.154045, 2022.

956   Jenkin, M. E., Young, J. C., and Rickard, A. R.: The MCM v3.3.1 degradation
957 scheme for isoprene, Atmos. Chem. Phys., 15, 11433-11459, 10.5194/acp-15-11433-
958 2015, 2015.

959   Klein, A., Ravetta, F., Thomas, J. L., Ancellet, G., Augustin, P., Wilson, R.,
960 Dieudonné, E., Fourmentin, M., Delbarre, H., and Pelon, J.: Influence of vertical mixing
961 and nighttime transport on surface ozone variability in the morning in Paris and the
962 surrounding region, Atmos. Environ., 197, 92-102, 10.1016/j.atmosenv.2018.10.009,
963 2019.

964   Li, X.-B., Yuan, B., Wang, S., Wang, C., Lan, J., Liu, Z., Song, Y., He, X.,
965 Huangfu, Y., Pei, C., Cheng, P., Yang, S., Qi, J., Wu, C., Huang, S., You, Y., Chang,
966 M., Zheng, H., Yang, W., Wang, X., and Shao, M.: Variations and sources of volatile
967 organic compounds (VOCs) in urban region: insights from measurements on a tall
968 tower, Atmos. Chem. Phys., 22, 10567-10587, 10.5194/acp-22-10567-2022, 2022.

969   Li, X.-B., Zhang, C., Liu, A., Yuan, B., Yang, H., Liu, C., Wang, S., Huangfu, Y.,
970 Qi, J., Liu, Z., He, X., Song, X., Chen, Y., Peng, Y., Zhang, X., Zheng, E., Yang, L.,
971 Yang, Q., Qin, G., Zhou, J., and Shao, M.: Assessment of long tubing in measuring
972 atmospheric trace gases: applications on tall towers, Environ. Sci.: Atmos., 3, 506-520,
973 10.1039/d2ea00110a, 2023.

974   Li, Y., Liu, B., Ye, J., Jia, T., Khuzestani, R. B., Sun, J. Y., Cheng, X., Zheng, Y.,
975 Li, X., Wu, C., Xin, J., Wu, Z., Tomoto, M. A., McKinney, K. A., Martin, S. T., Li, Y.
976 J., and Chen, Q.: Unmanned aerial vehicle measurements of volatile organic
977 compounds over a subtropical forest in China and implications for emission
978 heterogeneity, ACS. Earth. Space. Chem., 5, 247-256,
979 10.1021/acsearthspacechem.0c00271, 2021.

980   Liang, X., Chen, X., Zhang, J., Shi, T., Sun, X., Fan, L., Wang, L., and Ye, D.:
981 Reactivity-based industrial volatile organic compounds emission inventory and its
982 implications for ozone control strategies in China, Atmos. Environ., 162, 115-126,
983 10.1016/j.atmosenv.2017.04.036, 2017.

984   Liu, J., Liu, Z., Ma, Z., Yang, S., Yao, D., Zhao, S., Hu, B., Tang, G., Sun, J.,
985 Cheng, M., Xu, Z., and Wang, Y.: Detailed budget analysis of HONO in Beijing, China:
986 Implication on atmosphere oxidation capacity in polluted megacity, Atmos. Environ.,
987 244, 117957, 10.1016/j.atmosenv.2020.117957, 2021.

988   Liu, T., Hong, Y., Li, M., Xu, L., Chen, J., Bian, Y., Yang, C., Dan, Y., Zhang, Y.,
989 Xue, L., Zhao, M., Huang, Z., and Wang, H.: Atmospheric oxidation capacity and
990 ozone pollution mechanism in a coastal city of southeastern China: analysis of a typical
991 photochemical episode by an observation-based model, Atmos. Chem. Phys., 22, 2173-
992 2190, 10.5194/acp-22-2173-2022, 2022.

993   Liu, X., Wang, N., Lyu, X., Zeren, Y., Jiang, F., Wang, X., Zou, S., Ling, Z., and
994 Guo, H.: Photochemistry of ozone pollution in autumn in Pearl River Estuary, South

China, Sci. Total Environ., 754, 141812, 10.1016/j.scitotenv.2020.141812, 2021.

Liu, Z., Zha, F., Wang, Y., Yuan, B., Liu, B., and Tang, G.: Vertical evolution of the concentrations and sources of volatile organic compounds in the lower boundary layer in urban Beijing in summer, Chemosphere, 332, 138767, 10.1016/j.chemosphere.2023.138767, 2023.

Lu, X., Hong, J., Zhang, L., Cooper, O. R., Schultz, M. G., Xu, X., Wang, T., Gao, M., Zhao, Y., and Zhang, Y.: Severe surface ozone pollution in China: a global perspective, Environ. Sci. Technol. Lett., 5, 487-494, 10.1021/acs.estlett.8b00366, 2018.

Luo, Y., Dou, K., Fan, G., Huang, S., Si, F., Zhou, H., Wang, Y., Pei, C., Tang, F., Yang, D., Xi, L., Yang, T., Zhang, T., and Liu, W.: Vertical distributions of tropospheric formaldehyde, nitrogen dioxide, ozone and aerosol in southern China by ground-based MAX-DOAS and LIDAR measurements during PRIDE-GBA 2018 campaign, Atmos. Environ., 226, 10.1016/j.atmosenv.2020.117384, 2020a.

Luo, Y. P., Fu, J. Y., Li, Q. S., Chan, P. W., and He, Y. C.: Observation of Typhoon Hato based on the 356-m high meteorological gradient tower at Shenzhen, J. Wind. Eng. Ind. Aerodyn., 207, 104408, 10.1016/j.jweia.2020.104408, 2020b.

Mao, J., Yan, F., Zheng, L., You, Y., Wang, W., Jia, S., Liao, W., Wang, X., and Chen, W.: Ozone control strategies for local formation- and regional transport-dominant scenarios in a manufacturing city in southern China, Sci. Total Environ., 813, 10.1016/j.scitotenv.2021.151883, 2022.

Mousavinezhad, S., Choi, Y., Pouyaei, A., Ghahremanloo, M., and Nelson, D. L.: A comprehensive investigation of surface ozone pollution in China, 2015–2019: Separating the contributions from meteorology and precursor emissions, Atmos. Res., 257, 10.1016/j.atmosres.2021.105599, 2021.

Pan, X., Kanaya, Y., Tanimoto, H., Inomata, S., Wang, Z., Kudo, S., and Uno, I.: Examining the major contributors of ozone pollution in a rural area of the Yangtze River Delta region during harvest season, Atmos. Chem. Phys., 15, 6101–6111, 10.5194/acp-15-6101-2015, 2015.

Parrish, D. D., Ryerson, T. B., Mellqvist, J., Johansson, J., Fried, A., Richter, D.,

Walega, J. G., Washenfelder, R. A., de Gouw, J. A., Peischl, J., Aikin, K. C., McKeen, S. A., Frost, G. J., Fehsenfeld, F. C., and Herndon, S. C.: Primary and secondary sources of formaldehyde in urban atmospheres: Houston Texas region, Atmos. Chem. Phys., 12, 3273-3288, 10.5194/acp-12-3273-2012, 2012.

Sadanaga, Y., Kawasaki, S., Tanaka, Y., Kajii, Y., and Bandow, H.: New system for measuring the photochemical ozone production rate in the atmosphere, Environ. Sci. Technol., 51, 2871-2878, 10.1021/acs.est.6b04639, 2017.

Salthammer, T.: Acetaldehyde in the indoor environment, Environ. Sci. Atmos., 3, 474-493, 10.1039/D2EA00146B, 2023.

Shen, H., Liu, Y., Zhao, M., Li, J., Zhang, Y., Yang, J., Jiang, Y., Chen, T., Chen, M., Huang, X., Li, C., Guo, D., Sun, X., Xue, L., and Wang, W.: Significance of carbonyl compounds to photochemical ozone formation in a coastal city (Shantou) in eastern China, Sci. Total Environ., 764, 10.1016/j.scitotenv.2020.144031, 2021.

Shi, J., Bao, Y., Ren, L., Chen, Y., Bai, Z., and Han, X.: Mass concentration, source and health risk assessment of volatile organic compounds in nine cities of Northeast China, Int. J. Environ. Res. Public Health, 19, 4915, 10.3390/ijerph19084915, 2022.

Spaulding, R. S., Schade, G. W., Goldstein, A. H., and Charles, M. J.: Characterization of secondary atmospheric photooxidation products: Evidence for biogenic and anthropogenic sources, J. Geophys. Res., 108, 4247, 10.1029/2002JD002478, 2003.

Sillman, S.: The relation between ozone, NOx and hydrocarbons in urban and polluted rural environments, Atmos. Environ., 33, 1821-1845, 10.1016/S1352-2310(98)00345-8, 1999.

Sklaveniti, S., Locoge, N., Stevens, P. S., Wood, E., Kundu, S., and Dusanter, S.: Development of an instrument for direct ozone production rate measurements: measurement reliability and current limitations, Atmos. Meas. Tech., 11, 741-761, 10.5194/amt-11-741-2018, 2018.

Steinfeld, J. I.: Atmospheric chemistry and physics: from air pollution to climate change, Environ. Sci. Policy. Sustain. Dev., 40, 26-26,

1055   10.1080/00139157.1999.10544295, 1998.

1056   Tan, Z., Lu, K., Jiang, M., Su, R., Wang, H., Lou, S., Fu, Q., Zhai, C., Tan, Q.,
1057   Yue, D., Chen, D., Wang, Z., Xie, S., Zeng, L., and Zhang, Y.: Daytime atmospheric
1058   oxidation capacity in four Chinese megacities during the photochemically polluted
1059   season: a case study based on box model simulation, Atmos. Chem. Phys., 19, 3493-
1060   3513, 10.5194/acp-19-3493-2019, 2019.

1061   Tan, Z., Lu, K., Dong, H., Hu, M., Li, X., Liu, Y., Lu, S., Shao, M., Su, R., Wang,
1062   H., Wu, Y., Wahner, A., and Zhang, Y.: Explicit diagnosis of the local ozone production
1063   rate and the ozone-NOx-VOC sensitivities, Sci. Bull., 63(16):1067-1076,
1064   10.1016/j.scib.2018.07.001, 2018.

1065   Tan, Z., Fuchs, H., Lu, K., Hofzumahaus, A., Bohn, B., Broch, S., Dong, H.,
1066   Gomm, S., Häseler, R., He, L., Holland, F., Li, X., Liu, Y., Lu, S., Rohrer, F., Shao, M.,
1067   Wang, B., Wang, M., Wu, Y., Zeng, L., Zhang, Y., Wahner, A., and Zhang, Y.: Radical
1068   chemistry at a rural site (Wangdu) in the North China Plain: observation and model
1069   calculations of OH, HO_2 and RO_2 radicals, Atmos. Chem. Phys., 17, 663-690,
1070   10.5194/acp-17-663-2017, 2017.

1071   Tang, G., Zhu, X., Xin, J., Hu, B., Song, T., Sun, Y., Zhang, J., Wang, L., Cheng,
1072   M., Chao, N., Kong, L., Li, X., and Wang, Y.: Modelling study of boundary-layer ozone
1073   over northern China - Part I: Ozone budget in summer, Atmos. Res., 187, 128-137,
1074   10.1016/j.atmosres.2016.10.017, 2017.

1075   Wang, C., Yuan, B., Wu, C., Wang, S., Qi, J., Wang, B., Wang, Z., Hu, W., Chen,
1076   W., Ye, C., Wang, W., Sun, Y., Wang, C., Huang, S., Song, W., Wang, X., Yang, S.,
1077   Zhang, S., Xu, W., Ma, N., Zhang, Z., Jiang, B., Su, H., Cheng, Y., Wang, X., and Shao,
1078   M.: Measurements of higher alkanes using NO^+ chemical ionization in PTR-ToF-MS:
1079   important contributions of higher alkanes to secondary organic aerosols in China,
1080   Atmos. Chem. Phys., 20, 14123–14138, 10.5194/acp-20-14123- 2020, 2020.

1081   Wang, N., Lyu, X., Deng, X., Huang, X., Jiang, F., and Ding, A.: Aggravating O_3
1082   pollution due to NOx emission control in eastern China, Sci. Total Environ., 677, 732-
1083   744, 10.1016/j.scitotenv.2019.04.388, 2019.

1084   Wang, P., Chen, Y., Hu, J., Zhang, H., and Ying, Q.: Attribution of tropospheric
1085   ozone to NOx and VOC Emissions: considering ozone formation in the transition

regime, Environ. Sci. Technol., 53, 1404-1412, 10.1021/acs.est.8b05981, 2019.

Wang, Y., Zhang, Y., Hao, J., and Luo, M.: Seasonal and spatial variability of surface ozone over China: contributions from background and domestic pollution, Atmos. Chem. Phys., 11, 3511-3525, 10.5194/acp-11-3511-2011, 2011.

Wang, W., Parrish, D. D., Wang, S., Bao, F., Ni, R., Li, X., Yang, S., Wang, H., Cheng, Y., and Su, H.: Long-term trend of ozone pollution in China during 2014–2020: distinct seasonal and spatial characteristics and ozone sensitivity, Atmos. Chem. Phys., 22, 8935-8949, 10.5194/acp-22-8935-2022, 2022a.

Wang, W., Yuan, B., Peng, Y., Su, H., Cheng, Y., Yang, S., Wu, C., Qi, J., Bao, F., Huangfu, Y., Wang, C., Ye, C., Wang, Z., Wang, B., Wang, X., Song, W., Hu, W., Cheng, P., Zhu, M., Zheng, J., and Shao, M.: Direct observations indicate photodegradable oxygenated volatile organic compounds (OVOCs) as larger contributors to radicals and ozone production in the atmosphere, Atmos. Chem. Phys., 22, 4117-4128, 10.5194/acp-22-4117-2022, 2022b.

Wang, W.; Yuan, B.; Su, H.; Cheng, Y.; Qi, J.; Wang, S.; Song, W.; Wang, X.; Xue, C.; Ma, C.; Bao, F.; Wang, H.; Lou, S.; Shao, M.: A large role of missing volatile organic compound reactivity from anthropogenic emissions in ozone pollution regulation, Atmos. Chem. Phys., 24, (7), 4017-4027,10.5194/acp-24-4017-2024, 2024.

Wang, X., Zhang, T., Xiang, Y., Lv, L., Fan, G., and Ou, J.: Investigation of atmospheric ozone during summer and autumn in Guangdong Province with a lidar network, Sci. Total Environ., 751, 10.1016/j.scitotenv.2020.141740, 2021.

Wang, Y., Guo, H., Zou, S., Lyu, X., Ling, Z., Cheng, H., and Zeren, Y.: Surface O_3 photochemistry over the South China Sea: Application of a near-explicit chemical mechanism box model, Environ. Pollut., 234, 155-166, 10.1016/j.envpol.2017.11.001, 2018.

Whalley, L. K., Stone, D., Dunmore, R., Hamilton, J., Hopkins, J. R., Lee, J. D., Lewis, A. C., Williams, P., Kleffmann, J., Laufs, S., Woodward-Massey, R., and Heard, D. E.: Understanding in situ ozone production in the summertime through radical observations and modelling studies during the Clean air for London project (ClearfLo), Atmos. Chem. Phys., 18, 2547-2571, 10.5194/acp-18-2547-2018, 2018.

Whalley, L. K., Slater, E. J., Woodward-Massey, R., Ye, C., Lee, J. D., Squires, F., Hopkins, J. R., Dunmore, R. E., Shaw, M., Hamilton, J. F., Lewis, A. C., Mehra, A., Worrall, S. D., Bacak, A., Bannan, T. J., Coe, H., Percival, C. J., Ouyang, B., Jones, R. L., Crilley, L. R., Kramer, L. J., Bloss, W. J., Vu, T., Kotthaus, S., Grimmond, S., Sun, Y., Xu, W., Yue, S., Ren, L., Acton, W. J. F., Hewitt, C. N., Wang, X., Fu, P., and Heard, D. E.: Evaluating the sensitivity of radical chemistry and ozone formation to ambient VOCs and NOx in Beijing, Atmos. Chem. Phys., 21, 2125-2147, 10.5194/acp-21-2125-2021, 2021.

Wolfe, G. M., Marvin, M. R., Roberts, S. J., Travis, K. R., and Liao, J.: The Framework for 0-D Atmospheric Modeling (F0AM) v3.1, Geosci. Model. Dev., 9, 3309-3319, 10.5194/gmd-9-3309-2016, 2016.

World Meteorological Organization, Greenhouse Gas Bulletin No. 18, 2022, https://library.wmo.int/idurl/4/59137.

Wu, C., Wang, C., Wang, S., Wang, W., Yuan, B., Qi, J., Wang, B., Wang, H., Wang, C., Song, W., Wang, X., Hu, W., Lou, S., Ye, C., Peng, Y., Wang, Z., Huangfu, Y., Xie, Y., Zhu, M., Zheng, J., Wang, X., Jiang, B., Zhang, Z., and Shao, M.: Measurement report: Important contributions of oxygenated compounds to emissions and chemistry of volatile organic compounds in urban air, Atmos. Chem. Phys., 20, 14769–14785, 10.5194/acp-20-14769-2020, 2020.

Xue, L. K., Wang, T., Gao, J., Ding, A. J., Zhou, X. H., Blake, D. R., Wang, X. F., Saunders, S. M., Fan, S. J., Zuo, H. C., Zhang, Q. Z., and Wang, W. X.: Ground-level ozone in four Chinese cities: precursors, regional transport and heterogeneous processes, Atmos. Chem. Phys., 14, 13175-13188, 10.5194/acp-14-13175-2014, 2014.

Yang, S., Yuan, B., Peng, Y., Huang, S., Chen, W., Hu, W., Pei, C., Zhou, J., Parrish, D. D., Wang, W., He, X., Cheng, C., Li, X. B., Yang, X., Song, Y., Wang, H., Qi, J., Wang, B., Wang, C., Wang, C., Wang, Z., Li, T., Zheng, E., Wang, S., Wu, C., Cai, M., Ye, C., Song, W., Cheng, P., Chen, D., Wang, X., Zhang, Z., Wang, X., Zheng, J., and Shao, M.: The formation and mitigation of nitrate pollution: comparison between urban and suburban environments, Atmos. Chem. Phys., 22, 4539-4556, 10.5194/acp-22-4539-2022, 2022.

Yang, W., Chen, H., Wang, W., Wu, J., Li, J., Wang, Z., Zheng, J., and Chen, D.:

Modeling study of ozone source apportionment over the Pearl River Delta in 2015, Environ. Pollut., 253, 393-402, 10.1016/j.envpol.2019.06.091, 2019.

Yuan, B., Chen, W., Shao, M., Wang, M., Lu, S., Wang, B., Liu, Y., Chang, C.-C., and Wang, B.: Measurements of ambient hydrocarbons and carbonyls in the Pearl River Delta (PRD), China, Atmos. Res., 116, 93-104, 10.1016/j.atmosres.2012.03.006, 2012.

Yuan, B., Koss, A. R., Warneke, C., Coggon, M., Sekimoto, K., and de Gouw, J. A.: Proton-Transfer-Reaction Mass Spectrometry: applications in atmospheric sciences, Chem. Rev., 117, 13187–13229, 10.1021/acs.chemrev.7b00325, 2017.

Zhao, W., Tang, G., Yu, H., Yang, Y., Wang, Y., Wang, L., An, J., Gao, W., Hu, B., Cheng, M., An, X., Li, X., and Wang, Y.: Evolution of boundary layer ozone in Shijiazhuang, a suburban site on the North China Plain, J. Environ. Sci., 83, 152-160, 10.1016/j.jes.2019.02.016, 2019.

Zhang, X., Xu, J., Kang, S., Zhang, Q., and Sun, J.: Chemical characterization and sources of submicron aerosols in the northeastern Qinghai–Tibet Plateau: insights from high-resolution mass spectrometry, Atmos. Chem. Phys., 19, 7897-7911, 10.5194/acp-19-7897-2019, 2019.

Zhang, Y., Zhang, Y., Liu, Z., Bi, S., and Zheng, Y.: Analysis of vertical distribution changes and influencing factors of tropospheric ozone in China from 2005 to 2020 based on multi-source data, Int. J. Environ. Res. Public Health, 19, 10.3390/ijerph191912653, 2022.

Zhou, J.; Wang, W.; Wu, Y.; Zhang, C.; Liu, A.; Hao, Y.; Li, X.-B.; Shao, M.: Development and application of a nitrogen oxides analyzer based on the cavity attenuated phase shift technique, J. Environ. Sci., 150, 692-703, 10.1016/j.jes.2023.11.017, 2025.

Zhou, J., Yuan, B., Li, X., and Shao, M.: Measurement and modelling results of O_3 and its precursors [Data set]. Zenodo. 10.5281/zenodo.7854639, 2023.

Zhu, H., Wang, H., Jing, S., Wang, Y., Cheng, T., Tao, S., Lou, S., Qiao, L., Li, L., and Chen, J.: Characteristics and sources of atmospheric volatile organic compounds (VOCs) along the mid-lower Yangtze River in China, Atmos. Environ.,

1177   190, 232-240, 10.1016/j.atmosenv.2018.07.026 2018.

1178   Zhu, J., Wang, S., Wang, H., Jing, S., Lou, S., Saiz-Lopez, A., and Zhou, B.:
1179   Observationally constrained modeling of atmospheric oxidation capacity and
1180   photochemical reactivity in Shanghai, China, Atmos. Chem. Phys., 20, 1217-1232,
1181   10.5194/acp-20-1217-2020, 2020.

1182

1183

1184

1185